

Calculus with combinatorial differential forms for fluid flow analysis in porous and fractured media

Changhao Liu^{a,*}, Kiprian Berbatov^a, Majid Sedighi^b, Andrey P. Jivkov^{a,**}

^a*Department of Mechanical and Aerospace Engineering, The University of Manchester, Oxford Road, Manchester M13 9PL, UK*

^b*Department of Civil Engineering and Management, The University of Manchester, Oxford Road, Manchester M13 9PL, UK*

Abstract

The fabric of porous and fractured media contains solid regions (grains) and voids. The space conducting fluids is a system of connected voids with variable geometries. Relative to the grain sizes, the voids can be voluminous with three comparable large extensions, narrow expansive with two comparable large extensions and one smaller extension, and thin long with one comparable large extension and two smaller extensions. The widely used representation of void spaces by systems of spheres connected by cylinders (pore network models) is an acceptable approximation for some special cases, but not for most porous and fractured media. We propose a flexible method for modelling such media by mapping their measured fabric's characteristics – void and grain volume distributions and shapes – onto polyhedral tessellations of space. The map assigns voluminous voids and grains to polyhedrons (3D), narrow expansive voids to some polyhedral faces (2D), and thin long voids to some polyhedral edges (1D), as dictated by experimental data. The analysis of transport through such discrete structures with components of different dimensions is performed by a novel mathematical method, which uses combinatorial differential forms to represent physical properties and their fluxes, as well as structure-preserving operators on such forms to formulate the conservation laws exactly and directly in matrix form, ready for computation. The method allows for individual material properties, such as conductivity, to be assigned to voids of all dimensions, so that the three types of voids are suitably represented. Publicly available XCT images of four different rocks are used to test the method. Image analysis is used to obtain their fabrics' characteristics and 30 model realisations with a statistically equivalent fabric are constructed for each rock. The new mathematical method is used to calculate a range of realisation-dependent permeabilities. Fluid dynamics simulations in the imaged pore spaces are performed to obtain a single, image-dependent, permeability for each rock. The results demonstrate the ability of the proposed method to predict the spread of transport coefficients for a given fabric using only fabric's statistical characteristics. They agree with experimentally measured and calculated by fluid dynamics permeabilities. The key benefits are the significantly lower computational cost compared to fluid dynamics simulations, the opportunity for up-scaling to large rock volumes with sufficiently accurate fabric's statistics, and the potential for investigating the effect of pore space evolution on transport properties.

Keywords: Porous media, Fractured rock, Discrete model, Fluid flow, Permeability

1. Introduction

Developing a method for calculating fluid flow in porous and fractured materials is a challenging task. The classical formulation is based on the approximation of these materials as continuous media [1]. In such case, a scalar physical property, fluid volume, is represented by a scalar density field, continuously distributed over the points of a material domain. The volume density is related to pressure via an equation of state. The pressure gradient is related to fluid flow velocity via a constitutive relation (Darcy's law). The flow continuity at material points is given by the divergence of the flow velocity, leading to a partial differential equation (PDE) for volume density. This formulation can only be used at engineering length scales where materials are sufficiently well approximated as continua. Fluid flow can then be simulated by established numerical methods for solving PDEs, such as finite elements [2] or finite volumes [3], with macroscopic/bulk material properties.

The properties of real materials, however, are non-uniformly distributed; in fact, they are discontinuously distributed in porous and fractured media, e.g., between the solid phase and the pore space [4]. The macroscopic/bulk properties are emergent, i.e., they depend on the arrangements (fabric) and interactions of internal microstructural elements [5]. The direct approaches to obtain the bulk properties are by experiments at larger length scales and by simulations of fluid flow in the segmented pore space from X-ray Computed Tomography (XCT) images at smaller length scales. In both cases, the values will depend on the fabric of the test pieces. A large material domain will require multiple experiments or imaging and simulations with different test pieces to determine the range of fabric-dependent values. The experiments and the imaging, as well as the classic simulation method, Computational Fluid Dynamics (CFD), are expensive to conduct in large numbers.

*Corresponding author: changhao.liu-2@postgrad.manchester.ac.uk

**Corresponding author: andrey.jivkov@manchester.ac.uk

Bulk properties are also derived in engineering practice using approximate relations to some averaged pore space characteristics, such as porosity, tortuosity, and pore surface area [6, 7]. A typical example of such a relation is the Kozeny-Carman equation [8], which has been widely used in the porous media community and has been modified several times [9, 10]. Irrespective of the way bulk properties are obtained, the return to the continuum description can only serve engineering scale simulations. It cannot provide understanding of the effect of the fabric on the emergent behaviour, and critically the effect of fabric evolution on this behaviour. Such understanding requires a discrete representation of the pore space that reflects as closely as possible its measured characteristics.

Conceptually, the simplest approach to consider the pore space discreteness, thus allowing for analysis of fabric effect on emergent behaviour, is the pore network modelling (PNM) [11, 12]. In PNM, pores are represented by spherical containers with sizes following measured pore size distribution, connected by throats represented by cylinders with sizes following measured throat size distribution. Thus, the flow is 1-dimensional along the throats and the mass conservation is established in pores. However, real pore spaces are rarely amenable to pore network representations, which is evidenced by markedly different pore networks constructed directly from XCT images by different characterisation algorithms [13]. In fact, typical pore spaces are collections of features that appear to have different dimensions. This can be observed in the recently reported database of imaged rocks [14]. For example, some pores are elongated in one direction, as cylinders/rods, while others are elongated in two directions, as plates/blades (this category includes fractures). Relative to the 3D grains, the former appear as 1D and the latter as 2D features. The classification of pore shapes can be done by the parameter compactness related to three axial lengths of pores [4, 15]. Capturing this complexity requires a different approach to representation and analysis of porous and fractured media to underpin the advance in understanding the effects of fabric and its evolution on fluid flow. Such an approach should capture the finite, discrete natures/properties of pore space components and be capable of computing its multi-dimensional interactions between internal elements.

The aim of this paper is to demonstrate how a new mathematical description of the fabric of porous and fractured media as a collection of discrete entities of different dimensions, together with a new calculus on such collections, provides the essential flexibility to model fabrics of arbitrary complexity and to calculate fluid flow and their macroscopic transport properties effectively and efficiently. In Section 2 we present the mathematical formalism for describing collections of discrete entities and for analysis of their behaviour. In Section 3, we provide the fabric characteristics of four rocks obtained by analyses of publicly available XCT images and show how these are mapped to the elements of collections to construct statistically representative models. In Section 4, we show the results of fluid flow analysis with the new method and compare these with fluid dynamics simulations performed on the imaged pore spaces to demonstrate the accuracy and efficiency of the proposed approach.

2. Description and analysis of porous media

The development of a method for description and analysis of complex materials' systems involves mathematical concepts that are not yet included in the mainstream mathematical education (exterior calculus) or are a recent development (calculus with combinatorial differential forms). Therefore, we provide an incremental introduction to these concepts as illustrated in Figure 1. Our aim is to arrive at the bottom right block of the diagram by building the required language and operations. It is assumed that the reader is familiar with vector calculus, so this block is not discussed.

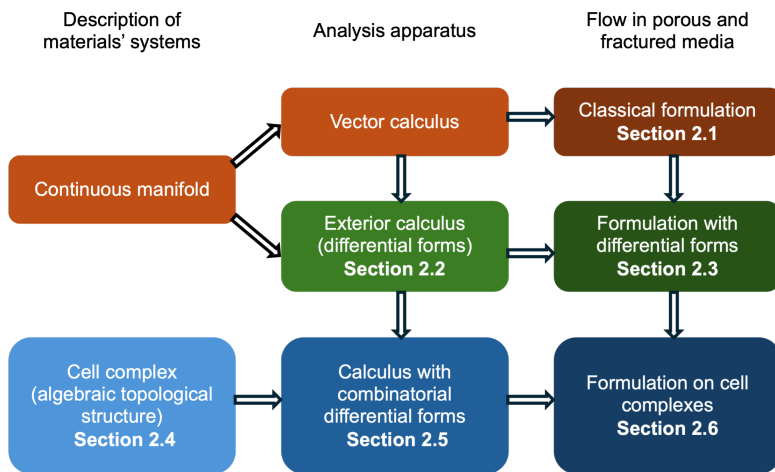


Figure 1: Pathway for development of calculus on complex materials' systems

2.1. Classical formulation

The continuum formulation of fluid flow in porous media is based on the approximation of a porous body by a collection of infinitely many infinitesimal points, \mathbf{x} , occupying a region $M \subset \mathbb{R}^3$ with boundary ∂M . The fluid volume

density, $\rho(\mathbf{x})$, and the porosity (pore volume fraction), $\phi(\mathbf{x})$, are continuously distributed scalar fields, and the fluid velocity, $\mathbf{v}(\mathbf{x})$, is a continuously distributed vector field over M . The flow continuity at all $\mathbf{x} \in M$ is given by

$$\frac{\partial(\rho\phi)}{\partial t} + \nabla \cdot (\rho\mathbf{v}) = 0, \quad (1)$$

and the equation of fluid motion is given by

$$\mathbf{v} = -\frac{k}{\mu} \nabla p, \quad (2)$$

where p is the fluid pressure, k is a pore space structure parameter referred to as the permeability, and μ is the fluid dynamic viscosity. Equation (2) is the velocity version of the Darcy's law relating the volumetric flow rate to the gradient of pressure. The permeability is a tensorial quantity that can be a spherical tensor for isotropic media, or a general tensor for fully anisotropic media. We will refer to the ratio $K = k/\mu$ as the conductivity. It is related to the engineering hydraulic conductivity via $K_h = K g \rho$, where g is the gravitational acceleration. The pressure is related to fluid density and porosity via equations of state for the fluid and the solid parts of the system, respectively, which contain material parameters – compressibility of fluid, C_F , and of solid, C_S . For elastic transient flow the substitution of eq. (2) into eq. (1) and considering the equations of state leads to (see, e.g., [16]):

$$\frac{\partial(Cp)}{\partial t} = \nabla \cdot (K \nabla p). \quad (3)$$

where $C = \phi C_F + C_S$ is the total compressibility of the porous medium. The quantities of interest and their physical dimensions are summarised in Table 1. Note that M denotes mass, L denotes length, and T denotes time.

Table 1: Quantities in the classical continuum formulation of flow in porous media

Quantity	Symbol	Physical dimension	Field type
fluid pressure	p	$\text{ML}^{-1}\text{T}^{-2}$	scalar
fluid velocity	\mathbf{v}	LT^{-1}	vector
fluid density	ρ	ML^{-3}	scalar
porosity	ϕ	1	scalar
permeability	k	L^2	scalar/tensor
dynamic viscosity	μ	$\text{ML}^{-1}\text{T}^{-1}$	scalar
conductivity	K	$\text{M}^{-1}\text{L}^3\text{T}$	scalar/tensor
compressibility of fluid/solid/total	$C_F/C_S/C$	M^{-1}LT^2	scalar

Initial-boundary value problems are constructed by prescription of initial and boundary conditions. The initial condition is a scalar function $p_0(\mathbf{x})$ prescribing the fluid pressure at time $t = 0$ at all $\mathbf{x} \in M$, i.e., $p_0(\mathbf{x}) = p(\mathbf{x}, t = 0)$. The boundary ∂M is partitioned into two non-overlapping parts Γ_D and Γ_N , where Dirichlet and Neumann boundary conditions are prescribed by scalar functions $\tilde{p}(\mathbf{x}, t)$ and $\tilde{v}(\mathbf{x}, t)$, respectively, so that: $p(\mathbf{x}, t) = \tilde{p}(\mathbf{x}, t)$, for $\mathbf{x} \in \Gamma_D$, and $\mathbf{v}(\mathbf{x}, t) \cdot \mathbf{n} = \tilde{v}(\mathbf{x}, t)$, for $\mathbf{x} \in \Gamma_N$, where \mathbf{n} is the outer unit normal to Γ_N .

In the following sub-sections we will describe the discrete analogues of all quantities and operations involved in the formulation of fluid flow and will arrive at a background-independent formulation of this process. Our approach is based on ideas from the smooth exterior calculus developed by Élie Cartan in 1899 [17]. Therefore, we will make a quick overview of this calculus, before introducing its discrete analogue and the discrete formulation.

2.2. Overview of exterior calculus

Exterior calculus is an intrinsic (i.e., coordinate-independent) and metric-independent theory which forms the backbone of modern differential geometry. It is a versatile theory that vastly generalises vector calculus by giving much more structured formalism for higher-dimensional calculus and geometry. It is based on differential forms and its two main ingredients include the algebraic exterior product, also referred to as the wedge product, and the analytic exterior derivative.

(Smooth) differential forms are the objects of integration, see, e.g., [18], with many applications in differential geometry, see, e.g., [19]. As such they form a rigorous counterparts of the lousily defined infinitesimal line, area, and volume elements from multi-variable calculus. A p -form on a manifold M is represented as a linear combination of terms of the form

$$f dx_{i_1} \wedge \dots \wedge dx_{i_p}, \quad (4)$$

for some function f on M and some multi-index $I = (i_1, \dots, i_p)$. The space of p -forms on M is denoted by $\Omega^p M$. On a smooth manifold of dimension 3 they interpret:

- a scalar field f as a differential 0-form f ;
- a vector field (P, Q, R) as a differential 1-form $P dx + Q dy + R dz$;
- a pseudo-vector field (P, Q, R) as a differential 2-form $P dy \wedge dz + Q dz \wedge dx + R dx \wedge dy$;

- a pseudo-scalar field f as a differential 3-form $f dx \wedge dy \wedge dz$.

The **(smooth) exterior product** \wedge of differential forms is an algebraic antisymmetric operation that takes a p -form ω and a q -form η and returns a $(p+q)$ -form $\omega \wedge \eta$, for non-negative integers p and q with $p+q \leq 3$. The main algebraic operations in vector calculus are interpreted as follows:

- multiplication of a vector field with a function is interpreted by the exterior product of a 0-form with a 1-form;
- dot product of vector fields is interpreted by the exterior product of a 1-form with a 2-form;
- cross product of vector fields is interpreted by the exterior product of a 1-form with a 1-form.

Note that $\eta \wedge \omega = (-1)^{pq} \omega \wedge \eta$ and so all exterior products have interpretations back in vector calculus.

The **(smooth) exterior derivative** d of a differential form is an analytic operation that takes a p -form and returns a $(p+1)$ -form. The main differential operators in vector calculus are interpreted as follows:

- the gradient as the exterior derivative of a 0-form;
- the curl as the exterior derivative of a 1-form;
- the divergence as the exterior derivative of a 2-form.

The operator d satisfies the rule $d \circ d = 0$ and generalises the identities $\text{curl} \circ \text{grad} = 0$ and $\text{div} \circ \text{curl} = 0$.

Integration of differential forms assigns a real number to an oriented p -dimensional submanifold S and a p -form ω , denoted by $\int_S \omega$. It generalises single, multiple, line and surface integrals. If ∂S denotes the oriented boundary of S , then the *generalised Stokes' theorem* (or *Stokes-Cartan theorem*) states that

$$\int_{\partial S} \omega = \int_S d\omega \quad (5)$$

for a $(p-1)$ -form ω . It generalises the following theorems:

- Green's theorem for gradient ($p = 1$);
- Kelvin-Stokes theorem for curl ($p = 2$);
- Gauss's theorem for divergence ($p = 3$).

The operations discussed so far, exterior product, exterior derivative, and integration, do not depend on any notion of metric, although they interpret operations of vector calculus. A procedure for interchanging p -forms with $(3-p)$ -forms is needed to create an analogue of interchanging scalar with pseudo-scalar and vector with pseudo-vector fields in vector calculus. This requires the introduction of a **metric tensor**, fundamental in *Riemannian geometry*, which is used in the construction of inner product of forms, Hodge star operators between forms and co-differentials.

The **inner product of differential forms** assigns a real number to p -forms ω and η , denoted by $\langle \omega, \eta \rangle$. The **Hodge star operator** takes a p -form ω and returns a $(3-p)$ -form $\star \omega$. Hodge star operator satisfies $\star \star \omega = \omega$ and interprets the identification of scalar with pseudo-scalar fields by identifying 0- with 3-forms, and of vector with pseudo-vector fields by identifying 1- with 2-forms. The Hodge-star and inner product are related by the equation

$$\int_M (\omega \wedge \eta) = \langle \omega, \star \eta \rangle \quad (6)$$

for a p -form ω and a $(3-p)$ -form η . In our case the Euclidean metric is chosen, which leads to the following equalities:

- a 0-form $\omega := f$ and a 3-form $\eta := f dx \wedge dy \wedge dz$ are related by $\star_0 \omega = \eta$, $\star_3 \eta = \omega$;
- a 1-form $\omega := P dx + Q dy + R dz$ and a 2-form $\eta := P dy \wedge dz + Q dz \wedge dx + R dx \wedge dy$ are related by $\star_1 \omega = \eta$, $\star_2 \eta = \omega$;

The **codifferential** d^\star takes a p -form and returns a $(p-1)$ -form. Applied to a $(3-p)$ -form ω , it satisfies the equation

$$d_p^\star (\star_{3-p} \omega) = (-1)^p \star_{4-p} (d_{3-p} \omega). \quad (7)$$

By this definition it is easy to see that d_1^\star can be used to define the analogue of divergence on a 1-form.

2.3. Exterior calculus formulation of fluid flow

Consider the right-hand side of eq. (3). The pressure p can be represented as a 0-form, and its gradient is substituted with the differential d_0 which leads to a 1-form $d_0 p$. The conductivity K transforms $d_0 p$ to a 1-form

$$u := K d_0 p, \quad (8)$$

which is an analogue of the fluid velocity. (More precisely, the fluid velocity \mathbf{v} is the *sharp* of u , where sharp is the musical isomorphism from 1-forms to vector fields, induced by the inner product.) As we previously said, the analogue of divergence on forms is d_2 . In order to apply d_2 , the 1-form u has to be transformed into the *volumetric flow rate* 2-form $Q[\text{L}^3\text{T}^{-1}]$,

$$Q := \star_1 u. \quad (9)$$

If S is a oriented surface, then $\int_S Q$ represents the amount of volume flowing through S at a unit of time. Finally, the resulting 3-form $d_2 Q$ is transformed back into a 0-form using \star_3 . As a result, the analogue of divergence on 1-forms, applied to u^1 is the operator $\star_3 \circ d_2 \circ \star_1 = -d_1^*$. This leads to the following exterior calculus analogue of eq. (3):

$$\frac{\partial(Cp)}{\partial t} = -d_1^* K d_0 p. \quad (10)$$

In this formulation there is no change in the way the initial condition and the Dirichlet boundary condition are imposed. The Neumann boundary condition, on the other hand, is imposed as

$$\text{tr}_{\Gamma_N} Q = q(x, t), \quad (11)$$

where $q(x, t) \in \Omega^2 \Gamma_N$ is the volumetric flow rate through the Neumann boundary Γ_N , tr_{Γ_N} is the restriction operator of a form on M to a form on Γ_N (more precisely, it is the pullback of the inclusion map from Γ_N to M). Table 2 summarises the quantities participating in the governing equations in exterior calculus version. Note that in this model the quantity that expresses the fluid flow is the physically meaningful volumetric flow rate Q (albeit represented by its dual u), and not the fluid velocity \mathbf{v} . Precisely, they are related by $\mathbf{v} = u^\sharp = (\star_2 Q)^\sharp$, where \sharp is the *musical isomorphism* that maps 1-forms into vector fields.

Table 2: Quantities in the exterior calculus formulation of flow in porous media

Quantity	Symbol	Physical dimension	Domain
fluid pressure	p	$\text{ML}^{-1}\text{T}^{-2}$	$\Omega^0 M$
volumetric flow rate	Q	L^3T^{-1}	$\Omega^2 M$
dual volumetric flow rate	u	L^2T^{-1}	$\Omega^1 M$
conductivity	K	$\text{M}^{-1}\text{L}^3\text{T}$	$\Omega^1 M \rightarrow \Omega^1 M$
compressibility	C	M^{-1}LT^2	$\Omega^0 M \rightarrow \Omega^0 M$

In the following sub-sections we will present the discrete analogue of this exterior calculus formulation – conservation law eq. (10), supplied with initial, Dirichlet, and Neumann (eq. (11)) conditions.

2.4. Discrete representation of porous and fractured media

The smooth exterior calculus introduced briefly in Section 2.2 generalises the vector calculus and can replace it in modelling continuous media as shown in Section 2.3. However, as discussed in the introduction, porous and fractured media have complex microstructures, and our aim is to capture the complexity as closely as possible. For this we first need an appropriate mathematical description of microstructures and a discrete analogue of the smooth exterior calculus to represent the processes in such microstructures.

A material body with given internal structure can be described as a **cell complex** (or **mesh**) in the terminology of algebraic topology. A cell complex \mathcal{M} of dimension 3, consists of p -cells, $0 \leq p \leq 3$, and let N_p denote the number of p -cells in \mathcal{M} . For $p = 0, 1, 2, 3$, the p -cells represent nodes (cells of dimension 0), edges (cells of dimension 1), surface patches (cells of dimension 2), and bulk regions (cells of dimension 3), respectively. We will denote arbitrary p -cells by a_p, b_p, c_p . The topological **boundary** of c_p is a union of $0, 1, \dots, (p-1)$ -cells. For $q < p$, if b_q is on the boundary of c_p , we write $b_q \prec c_p$. Several notions from algebraic topology are essential for our consideration.

A **p -chain** is a formal linear combination of p -cells in \mathcal{M} . Thus, the space of all p -chains, denoted by $C_p \mathcal{M}$, has the set of p -cells in \mathcal{M} as a standard basis. Hence, we will denote basis chains in $C_p \mathcal{M}$ by the same letters as for p -cells. An arbitrary p -chain is a linear combination of basis p -chains, and we will use letters σ_p, τ_p for them. The **relative orientations** assign ± 1 to pairs $(c_p \succ b_{p-1})$ of p -cells and their $(p-1)$ -dimensional boundary cells, denoted by $\varepsilon(c_p, b_{p-1})$. The assignment of relative orientations on M is not unique (see Appendix B in the [supplementary material](#) of [20] for a particular way of building it), it just needs to make sure that the two adjacent 0-cells of a 1-cell are opposite to one another, and makes the boundary operator ∂ , defined shortly, satisfying $\partial^2 = 0$. However, it is important to note that we assume that \mathcal{M} is **compatibly oriented** in the sense that the relative orientations between any two adjacent volumes (3-cells) and their common 2-cell are opposite to one another. It is also helpful to assume

that the boundary $\partial\mathcal{M}$ of \mathcal{M} is compatibly oriented, i.e., adjacent 2-cells on $\partial\mathcal{M}$ have opposite relative orientations with their common 1-cell.

The **boundary operator** $\partial_p: C_p\mathcal{M} \rightarrow C_{p-1}\mathcal{M}$ is a linear map from p -chains to $(p-1)$ -chains, given by its action on an arbitrary basis p -chain c_p as

$$\partial_p c_p := \sum_{b_{p-1} \prec c_p} \varepsilon(c_p, b_{p-1}) b_{p-1}, \quad (12)$$

and extended by linearity on all p -chains. In the standard basis of basis chains, ∂_p is a sparse matrix with dimension $N_{p-1} \times N_p$ and nonzero values ± 1 representing relative orientations. The boundary operator satisfies the equation $\partial_p \circ \partial_{p+1} = 0$, i.e., the boundary of a boundary is empty, which in algebraic terminology means that the collection of spaces of p -chains, denoted by $C_\bullet\mathcal{M}$, forms, together with the boundary operator, a **chain complex** $(C_\bullet\mathcal{M}, \partial)$.

A linear function on p -chains is called a **p -cochain**. A p -cochain can be regarded as a function assigning a real number to each p -cell in \mathcal{M} . The p -cochains in \mathcal{M} form a vector space denoted by $C^p\mathcal{M}$ (the **linear-algebraic dual space** of $C^p\mathcal{M}$). In coordinates, a p -cochain is a column vector with dimension N_p . A basis p -cochain, corresponding to a cell c_p , is denoted by c^p , and is 1 when applied to c_p , and zero elsewhere. General p -cochain will be denoted by σ^p , τ^p .

The **linear-algebraic dual map** of ∂_{p+1} is the **coboundary operator** $\delta_p: C^p\mathcal{M} \rightarrow C^{p+1}\mathcal{M}$, which maps p -cochains to $(p+1)$ -cochains. Formally,

$$\delta_p \sigma^p := \sigma^p \circ \partial_{p+1}. \quad (13)$$

In the standard basis, δ_p is represented as a sparse matrix of dimension $N_{p+1} \times N_p$ and nonzero values ± 1 ; it is the transpose matrix of ∂_{p+1} . The coboundary operator satisfies the equation $\delta_{p+1} \circ \delta_p = 0$, i.e., the coboundary of coboundary is empty. This makes the collection of spaces of p -cochains, denoted by $C^\bullet\mathcal{M}$, together with the coboundary operator, a **cochain complex** $(C^\bullet\mathcal{M}, \delta)$.

The notions discussed so far are prevalent in algebraic topology and correspond to smooth exterior calculus in the following way:

- a cell complex \mathcal{M} is a finite version of the collection of all sub-manifolds of the ambient manifold M ;
- a chain in \mathcal{M} corresponds to a formal sum of oriented sub-manifolds of M ;
- the boundary operator ∂ on \mathcal{M} corresponds to the oriented boundary on chains in M ;
- cochains on \mathcal{M} correspond to smooth differential forms on M . In the “discretisation direction”, the **de Rham map** $R: \Omega^p M \rightarrow C^p\mathcal{M}$ is defined by

$$(R\omega^p)(c_p) := \int_{c_p} \omega^p, \quad (14)$$

where we interpret the integral over a basis chain c_p as integral over the ambient sub-manifold it occupies. In the opposite “interpolation direction” cochains are mapped to piecewise-smooth forms by the so-called **Whitney forms** (see, e.g., [21, Section 4] for simplicial and [22, Section 3.2.2] for cubical Whitney forms);

- the coboundary operator δ on \mathcal{M} corresponds to the smooth exterior derivative d on M . They are related by the equality

$$R \circ d = \delta \circ R. \quad (15)$$

A discrete analogue of the smooth wedge product, if it exists, is called the **cup product** of cochains. Cup products have been proposed for simplicial [21, Definition 5.1], cubical [22, Definition 3.2.1] and polygonal [23, Definition 3.2.4] meshes. However, we are not aware of discrete analogues of the wedge product for more general types of meshes, typically needed for faithful representation of materials’ internal structures. Therefore, we proceed in a different direction using Forman’s combinatorial differential forms [24] and Forman’s isomorphism between these forms and the cochains of an extended complex \mathcal{K} . This isomorphism allows to pull back a cup product of cochains on \mathcal{K} , if it exists, to a discrete wedge product of forms on \mathcal{M} . A larger class of \mathcal{M} topologies produce quasi-cubical \mathcal{K} , hence allow for a well defined cup product of cochains on \mathcal{K} , and thus a discrete wedge product of combinatorial forms on \mathcal{M} . Importantly, the combinatorial forms allow for more complex interactions between cells, which is essential for our purposes.

A **combinatorial differential q -form**, denoted by ω^q , is a mapping between cells. For $p \geq q$, ω^q maps a p -cell c_p to a linear combination of the $(p-q)$ -cells on the boundary of c_p . Thus, ω^q can be interpreted as an assignment of numbers to all pairs $(b_{p-q} \preceq c_p)$. The space of all q -forms will be denoted by $\Omega^q\mathcal{M}$. The **discrete exterior derivative** $D_q: \Omega^q\mathcal{M} \rightarrow \Omega^{q+1}\mathcal{M}$ is defined by [20, Definition 2.6]

$$D_q \omega^q := \omega^q \circ \partial - (-1)^p \partial \circ \omega. \quad (16)$$

(This definition differs by sign to the original [24, Definition 1.1].) It is easy to show [20, Proposition 2.8] that $D_{p+1} \circ D_p = 0$ which makes the space of all combinatorial differential forms, together with the discrete exterior derivative, a cochain complex, denoted by $(\Omega^\bullet\mathcal{M}, D)$. Forman [24, Theorem 1.2] proved that the **cohomology** of $(\Omega^\bullet\mathcal{M}, D)$ is isomorphic to the cohomology of $(C^\bullet\mathcal{M}, \delta)$, where δ is the coboundary operator on cochains in \mathcal{M} . He gave

an algebraic proof but sketched a geometric proof by building a subdivision \mathcal{K} of \mathcal{M} such that $(\Omega^\bullet \mathcal{M}, D) \cong (C^\bullet \mathcal{K}, \delta)$, where δ is the coboundary operator on cochains in \mathcal{K} . In such way, the combinatorial forms in \mathcal{M} are interpreted as cochains in \mathcal{K} , and the exterior derivative of forms in \mathcal{M} is given by the the coboundary operator in \mathcal{K} . This subdivision, referred to as the **Forman subdivision**, was later studied in [22, Chapter 5], referred to as the **kite complex**, again for topological purposes. Recently, the Forman subdivision was shown to be a suitable foundation for calculus on meshes and consequently for modelling materials with complex internal structures [20, Section 4]. The present work demonstrates its computational capabilities in modelling fluid flow in porous media. The Forman subdivision is built as follows:

- a p -cell in \mathcal{K} corresponds to a pair of a q -cell b_q in \mathcal{M} ($q \geq p$) and a $(q-p)$ -cell a_{q-p} on the boundary of b_q ; this cell is denoted by $(b_q \rightarrow a_{q-p})$
- the topology on \mathcal{K} , represented by the boundary relation \prec , is defined by considering the following cells in \mathcal{K} for $q > p$: a p -cell $\alpha_p := (c_r \rightarrow b_{r-p})$ and a q -cell $\beta_q := (d_s \rightarrow a_{s-q})$; then, by definition, $\alpha_p \prec \beta_q$ whenever $a_{s-q} \preceq b_{r-p}$ and $c_r \preceq d_s$;
- relative orientations in \mathcal{K} are defined by relative orientations in \mathcal{M} , see [20, Equation (2.3)];
- coordinates of nodes in \mathcal{K} can be defined in many ways: we use centroids of cells in \mathcal{M} .

The Forman subdivision is topologically unique. It is illustrated in Figure 2 on a small 2D triangular mesh. Note, that different colours in the subdivision correspond to pairs of different types in the original mesh. In \mathcal{M} nodes are in red, edges are in green, faces are in yellow. Correspondingly, nodes in \mathcal{K} are in red/green/orange respectively, depending on the type of cell they correspond to in \mathcal{M} . Edges in \mathcal{K} are in blue (corresponding to pairs $b_1 \succ a_0$) and in yellow (corresponding to pairs $b_2 \succ a_1$). Faces in \mathcal{K} are in pink, corresponding to pairs $b_2 \succ a_0$.

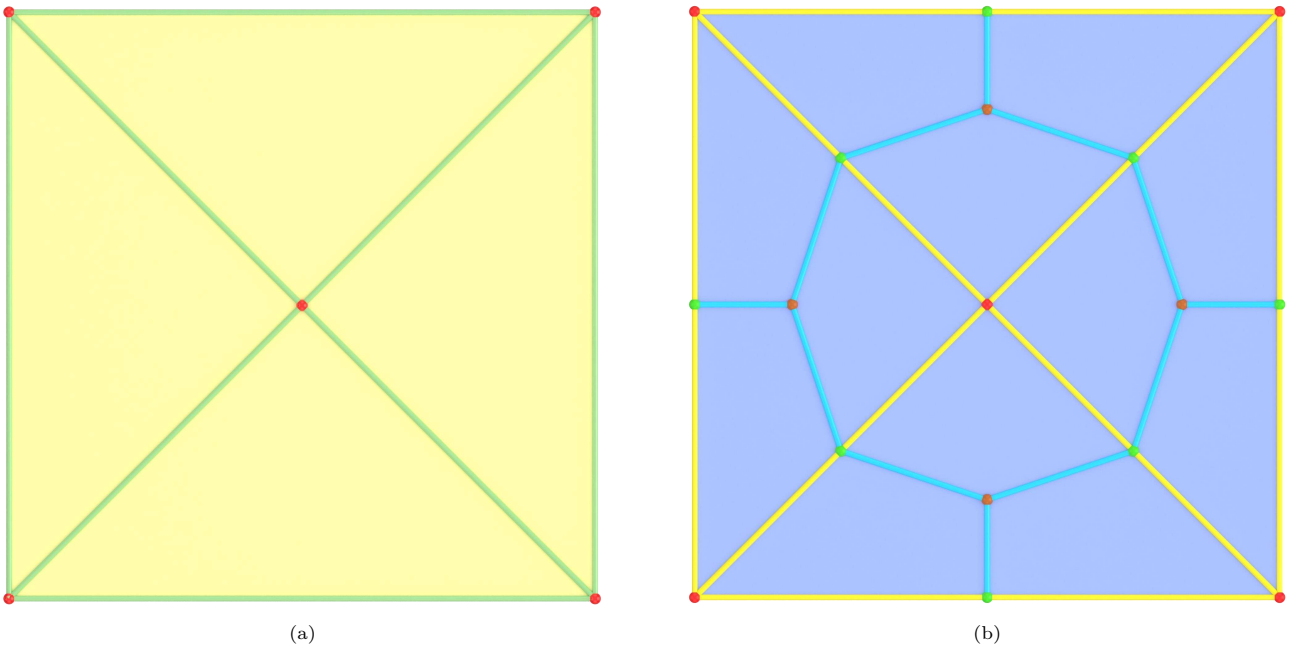


Figure 2: Triangular mesh \mathcal{M} (a) and its Forman subdivision \mathcal{K} (b)

In the 3D case, the construction leads to three types of 1-cells in \mathcal{K} : from 3-cells to 2-cells in \mathcal{M} corresponding to pairs $b_2 \prec c_3$; from 2-cells to 1-cells in \mathcal{M} corresponding to pairs $b_1 \prec c_2$; and from 1-cells to 0-cells in \mathcal{M} corresponding to pairs $b_0 \prec c_1$. If \mathcal{M} is a model of a material domain containing components of different apparent dimensions, the three types of 1-cells in \mathcal{K} allow for associating different properties to different dimensional components and for processes to operate simultaneously on all components. This means that voids and grains can be allocated to different dimensional cells according to their geometries, a marked computational advantage over the continuum theory. Furthermore, there are two types of 2-cells in \mathcal{K} : from 3-cells to 1-cells in \mathcal{M} representing pairs $b_1 \prec c_3$; and from 2-cells to 0-cells in \mathcal{M} representing pairs $b_0 \prec c_2$.

2.5. Calculus on quasi-cubical cell complexes

In the 3D case the extended complex \mathcal{K} consists of topological cubes (**quasi-cubes**) when \mathcal{M} is formed of simple polyhedrons, i.e., polyhedrons with 3 edges coming out of every vertex. The class of simple polyhedrons is large, including tetrahedrons, hexahedrons, and polyhedrons arising from space tessellations, such as Voronoi. On the quasi-cubes we apply the cup product \smile of [20, Definition 2.14], generalised from [22, Definition 3.2.1]. Since forms on \mathcal{M} are equivalent to cochains in \mathcal{K} , the cup product on \mathcal{K} is interpreted as a **discrete wedge product** on \mathcal{M} .

Two cells $b_{3-p}, c_p \in \mathcal{K}$ are **topologically orthogonal** if they share only one common 0-cell and are boundaries of a common 3-cells. This is written as $c_p \perp b_q$. The **discrete inner product** on \mathcal{K} is a bilinear form on $C^p\mathcal{K}$ such that basis cochains form an orthogonal basis, and for a p -cell c_p , [25, Equation (2.90)]

$$\langle c^p, c^p \rangle := \frac{1}{8\mu(c_p)} \sum_{b_{3-p} \perp c_p} \mu(b_{3-p}), \quad (17)$$

where $\mu(a_q)$ denotes the measure of the q -cell a_q (always 1 for $q = 0$, length for $q = 1$, area for $q = 2$, and volume for $q = 3$).

The **discrete Hodge star operator**, denoted by \star_p , is the unique operator satisfying [20, Definition 3.3]

$$(\tau^{3-p} \smile \sigma^p)[\mathcal{K}] = \langle \tau^{3-p}, \star_p \sigma^p \rangle, \quad (18)$$

for arbitrary cochains $\sigma^p \in C^p\mathcal{K}$ and $\tau^{3-p} \in C^{3-p}\mathcal{K}$. Here, $[\mathcal{K}]$ is the fundamental class of \mathcal{K} , i.e., the sum of all basis 3-cochains. Note, that the left hand side expresses a discrete form of integration. The discrete Hodge star \star_p is represented as a sparse matrix with dimension $N_{d-p} \times N_p$.

The **adjoint coboundary operator** δ_p^* is the discrete analogue of the codifferential. It is defined as the adjoint of δ_{p-1} with respect to the inner product [20, Definition 3.1], that is

$$\langle \sigma^p, \delta_{p-1} \tau^{p-1} \rangle = \langle \delta_p^* \sigma^p, \tau^{p-1} \rangle, \quad (19)$$

for arbitrary cochains $\sigma^p \in C^p\mathcal{K}$ and $\tau^{p-1} \in C^{p-1}\mathcal{K}$. The adjoint coboundary operator δ_p^* is represented as a sparse matrix with dimension $N_{p-1} \times N_p$ with the same stencil as the boundary operator ∂_p (only magnitudes of values differ from those of the boundary operator; the signs are the same).

The operations introduced above for the cochain spaces in \mathcal{K} are illustrated in Figure 3. Similarly to the interpretation of δ_0 , δ_1 , and δ_2 as gradient, curl, and divergence, of scalar, vector, and pseudo-vector fields, respectively, the adjoint coboundary operators δ_3^* , δ_2^* , and δ_1^* are interpreted as gradient, curl, and divergence, of pseudo-scalar, pseudo-vector, and vector fields, respectively. The relations between scalar and pseudo-scalar fields, and between vector and pseudo-vector fields are given by the Hodge-star operators. The algebraic representations of all discrete fields, i.e., all cochains, are 1-dimensional arrays, and the algebraic representations of all operators are 2-dimensional arrays (sparse matrices).

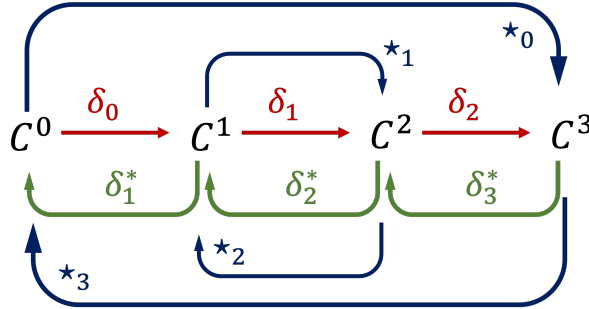


Figure 3: The cochain complex $(C^\bullet\mathcal{K}, \delta)$ and the metric-dependent operations on the cochain spaces.

2.6. Fluid flow in discrete media

The apparatus developed in Section 2.5 can be used for describing the problem of fluid flow based on the strong formulation given in Section 2.3 or on a weak (integral) formulation. Here we demonstrate the discrete version of the strong formulation.

The pressure p is represented by a 0-form on \mathcal{M} , i.e., pressure is defined for all cells in \mathcal{M} , hence it is a 0-cochain on \mathcal{K} . Let this cochain be denoted by π^0 . Further, the compressibility C is a material property that can be individually assigned to all cells in \mathcal{M} , so that $C = C_F$ or $C = C_S$ depending on whether the cell is associated with a void or a solid (see eq. (3)). This is transported as properties of 0-cells in \mathcal{K} , forming a diagonal matrix Π_0 with dimension $N_0 \times N_0$ of prescribed local compressibilities.

The exterior derivative of the pressure 0-form on \mathcal{M} gives the pressure differentials between pairs of cells ($d_0 \prec c_1$), ($c_1 \prec b_2$), and ($b_2 \prec a_3$) on \mathcal{M} . Correspondingly, $\delta_0 \pi^0$ gives a 1-cochain of pressure differentials on \mathcal{K} . These differentials drive the flow between the cells of the corresponding pairs, that is along 1-, 2-, or 3-cells in \mathcal{M} , with conductivities that can be different for different pairs depending on the local geometry. The local conductivities prescribed for transport between pairs in \mathcal{M} are transported as local conductivities of the 1-cells in \mathcal{K} , forming a diagonal matrix Π_1 with dimension $N_1 \times N_1$ of prescribed local conductivities. Define the 1-cochain v^1 on \mathcal{K} by (compare with eq. (8))

$$v^1 := \Pi_1 \delta_0 \pi^0. \quad (20)$$

v^1 does not relate to fluid velocity in a direct way, but like in the exterior calculus case its Hodge dual, $\psi^2 := \star_1 v^1$, is the discrete volumetric flow rate. More precisely, ψ^2 measures the fluid volumes passing the 2-cells per unit of time.

The discrete continuity equation is then represented in an analogous to eq. (10) way:

$$\frac{\partial(\Pi_0 \pi^0)}{\partial t} = -\delta_1^* v^1 = -\delta_1^* \Pi_1 \delta_0 \pi^0. \quad (21)$$

The action of δ_1^* restores the balance of spatial dimensions to provide the discrete analogue of $\Delta \cdot \mathbf{v}$. Equation (21) can also be written with a material-modified Laplacian $\tilde{\Delta}_0 := \delta_1^* \Pi_1 \delta_0$, which is a sparse matrix with dimension $N_0 \times N_0$:

$$\frac{\partial(\Pi_0 \pi^0)}{\partial t} = -\tilde{\Delta}_0 \pi^0. \quad (22)$$

Table 3 summarises the quantities participating in the governing equations of our discrete model (compare with Table 2).

Table 3: Quantities in the discrete formulation of flow in porous media

Quantity	Symbol	Physical dimension	Domain
fluid pressure	π^0	$\text{ML}^{-1}\text{T}^{-2}$	$C^0\mathcal{K}$
volumetric flow rate	ψ^2	L^3T^{-1}	$C^2\mathcal{K}$
dual volumetric flow rate	v^1	L^2T^{-1}	$C^1\mathcal{K}$
conductivity (diagonal matrix)	Π_1	$\text{M}^{-1}\text{L}^3\text{T}$	$C^1\mathcal{K} \rightarrow C^1\mathcal{K}$
compressibility (diagonal matrix)	Π_0	$\text{M}^{-1}\text{L}\text{T}^2$	$C^0\mathcal{K} \rightarrow C^0\mathcal{K}$

Initial-boundary value problems for eq. (21) on a material cell complex \mathcal{M} are prescribed as follows. The boundary $\partial\mathcal{M}$ contains cells of \mathcal{M} with dimensions less than 3, the boundary 2-cells and the edges and nodes they contain, and it itself is a 2-dimensional cell complex. Partition the set $(\partial\mathcal{M})_2$ of 2-cells of $\partial\mathcal{M}$ into (disjoint) Dirichlet and Neumann parts, respectively Σ_D^2 and Σ_N^2 . Take all lower-dimensional cells they contain to arrive to the 2-dimensional cell complexes Σ_D and Σ_N . Note that usually Σ_D and Σ_N will share common edges and nodes, where respective 2-cells intersect, unless they are on different connected components. The partitioning is transported to the boundary of \mathcal{K} , forming the sets Γ_D and Γ_N , such that for $p = 0, 1, 2$,

$$\Gamma_D^p := \{\alpha_p := c_q \rightarrow b_{q-p} \mid q \geq p, c_q \in \Sigma_D^q, b_{q-p} \preceq c_q\}, \quad (23)$$

$$\Gamma_N^p := \{\alpha_p := c_q \rightarrow b_{q-p} \mid q \geq p, c_q \in \Sigma_N^q, b_{q-p} \preceq c_q\}. \quad (24)$$

The conditions are prescribed as:

- Initial: for initial pressure p_0 on \mathcal{K} ,

$$\pi^0(c_0, 0) = p_0(c_0), c_0 \in \mathcal{K}_0 \cong \mathcal{M}. \quad (25)$$

- Dirichlet: for prescribed pressure p on Γ_D ,

$$\pi^0(c_0, t) = p(c_0, t), c_0 \in \Gamma_D^0, t \geq 0. \quad (26)$$

- Neumann (compare with eq. (11)): for prescribed volumetric flow rate f on Γ_N ,

$$\psi^2(c_2, t) = f(c_2, t), c_2 \in \Gamma_N^2, t \geq 0. \quad (27)$$

In our formulation, the number of unknowns at each time step is N_0 – the number of coefficient representing the pressure 0-cochain $\pi^0 \in C^0\mathcal{K}$. The equations available at each time step are: the conservation law for all internal nodes, Dirichlet condition for Dirichlet boundary, and Neumann condition for Neumann boundary. To achieve equal number of equations and unknowns, eq. (27) is modified for application on 0-cells, using the Hodge star operator

$$\star_{\Gamma_N, 2}: C^2\Gamma_N \rightarrow C^0\Gamma_N, \quad (28)$$

which follows the generic construction from [25]. Taking only the 0-cells in Γ_N that are not in Γ_D (Dirichlet condition is applied on common nodes), the Neumann boundary condition reduces to

$$(\star_{\Gamma_N, 2} \text{tr}_{\Gamma_N, 2} \star_1 \Pi_1 \delta_0 \pi^0)(c_0, t) = (\star_{\Gamma_N, 2} f)(c_0, t), c_0 \in \Gamma_N^0 \setminus \Gamma_D^0, \quad (29)$$

where $\text{tr}_{\Gamma_N, 2}$ is the restriction of a 2-form in \mathcal{K} to a 2-form on Γ_N . To summarise, denoting by \mathcal{K}_0° the set of internal nodes of \mathcal{K} , we get the the following problem for the unknown time-dependent 0-cochain π^0 :

$$\frac{\partial \Pi_0 \pi^0}{\partial t}(c_0, t) = -(\delta_1^* \circ \Pi_1 \circ \delta_0)(\pi^0)(c_0, t), \forall c_0 \in \mathcal{K}_0^\circ, t > 0 \quad [\text{T}^{-1}], \quad (30a)$$

$$\pi^0(c_0, t) = p(c_0, t), \forall c_0 \in \Gamma_D^0, t \geq 0 \quad [\text{ML}^{-1}\text{T}^{-2}], \quad (30b)$$

$$(\star_{\Gamma_N, 2} \circ \text{tr}_{\Gamma_N, 2} \circ \star_1 \circ \Pi_1 \circ \delta_0)(\pi^0)(c_0, t) = (\star_{\Gamma_N, 2} f)(c_0, t), \forall c_0 \in \Gamma_N^0 \setminus \Gamma_D^0, t \geq 0 \quad [\text{LT}^{-1}], \quad (30c)$$

$$\pi^0(c_0, 0) = p_0(c_0), \forall c_0 \in \mathcal{K}_0 \quad [\text{ML}^{-1}\text{T}^{-2}]. \quad (30d)$$

Solving eq. (30) requires a temporal numerical scheme, and then at each time leads to a linear system for the coefficients of π^0 . Imposing Dirichlet boundary conditions leads to exact numerical values for the coefficients of π^0 on the Dirichlet boundary. The remaining system, however, exhibits equations in different physical dimensions (namely, T^{-1} for conservation law and LT^{-1} for Neumann boundary condition), which is undesirable when forming the final left-hand side matrix and right-hand side vector. For this reason, we suggest for every $c_0 \in \Gamma_N^0 \setminus \Gamma_D^0$ to divide the corresponding row in the final system by the arithmetic mean of the adjacent edges of c_0 in Γ_N^1 . This will lead to a linear system $Ax = b$ with $N_0 - |\Gamma_D^0|$ unknowns and equations, where $A[\text{M}^{-1}\text{LT}]$, $x[\text{ML}^{-1}\text{T}^{-2}]$, $b[\text{T}^{-1}]$.

Hereafter, the proposed approach will be used for calculating the conductivity and permeability of models of porous and fractured media. For this purpose we mimic experimental setups with specimens of simple geometry (cuboids or cylinders) where pressures $p_1 < p_2$ are applied on two opposite parallel sides of equal areas A and at distance L , and the volumetric flow rate is measured. Typically, in such experiments the remaining sides of the specimens are insulated, i.e., the volumetric flow rate is zero. Solving the corresponding problem on a cell complex \mathcal{M} provides the volumetric flow rates across the 2-cells on the two opposite parallel boundaries with applied pressures. The conductivity is then calculated as in experiments by:

$$K = \frac{Q \cdot L}{(p_2 - p_1) \cdot A}, \quad (31)$$

where Q is the sum of volumetric flow rates across one boundary.

The solution to transient problems is performed by the implicit Euler method. The transient solutions converge to steady-state solutions in all cases, only the convergent times depend on the topological structure, geometry and material properties of \mathcal{M} . Since we are interested in calculating the conductivity, the results are obtained directly with steady-state solutions for computational efficiency. At steady-state, the sums of the volumetric flow rates at the two opposite sides are equal.

3. Materials and models

The application case studies presented in this section deal with fluid flow in a rock. Four different rocks are considered for demonstration of the proposed method: Bentheimer sandstone (BS), Doddington sandstone (DS), Estailades carbonate (EC), and Ketton carbonate (KC). These are typical geomaterials with random and complex pore system and grain size distribution, making them suitable for demonstrating the capabilities of the new method. Bulk properties and XCT images of the four rocks are obtained from the dataset of the Department of Earth Science and Engineering, Imperial College London: <https://www.imperial.ac.uk/earth-science/> [26, 27]. The bulk porosity and permeability of all rocks are given in Table 4. It can be seen from the data that the proportions between permeability and porosity vary significantly between different rocks, demonstrating that the porosity alone is not controlling the permeability. One needs to further consider the effects of pore shape and volume distribution for predicting permeability.

Table 4: Measured characteristics of rocks by bulk experiments

Material	Measured Helium porosity	Measured permeability (10^{-12} m^2)
Bentheimer sandstone	0.20	1.875
Doddington sandstone	0.192	1.038
Estailades carbonate	0.295	0.149
Ketton carbonate	0.2337	2.807

3.1. Material fabric's characteristics

We use the microCT images of DS, EC and KC (provided by the Imperial College London). BS image was provided by [iRock Technologies](#). It is noted that the imaged samples are different from the samples used for measuring the bulk properties. The raw data provided for each rock is an 8-bit unsigned image, where each voxel is represented by an 8-bit unsigned integer between 0 to 255. The sizes of all images are 1000 voxels in each spatial direction. We used Avizo 3D software (Thermo Fisher Scientific, USA) to perform image segmentation and microstructure characterisation. To avoid boundary effects, the images were cropped to 800 voxels in each direction. The segmentation of voids/pores and grains/particles was performed by the Avizo watershed segmentation algorithm with Gaussian filter and thresholding function. The segmented images are shown in Figure 4, where the coloured parts are voids. The voxel size and the void volume fraction calculated after segmentation are given in Table 5. A comparison with the porosities in Table 4 shows that a significant fraction of the helium-measured porosity in all rocks except the Bentheimer sandstone is not detectable with these voxel resolutions. This suggests that the permeability predictions of models constructed by data from the available images should not be compared with the experimentally measured bulk permeabilities. For this reason, comparisons will be made with fluid dynamics simulations in the imaged void spaces. The reconstructed material domains with coloured voids for the four rocks are shown in Figure 5. Different colours represent different ordinal numbers of voids. It can be observed in Table 4 and Figure 5 that all rocks contain voluminous grains, and

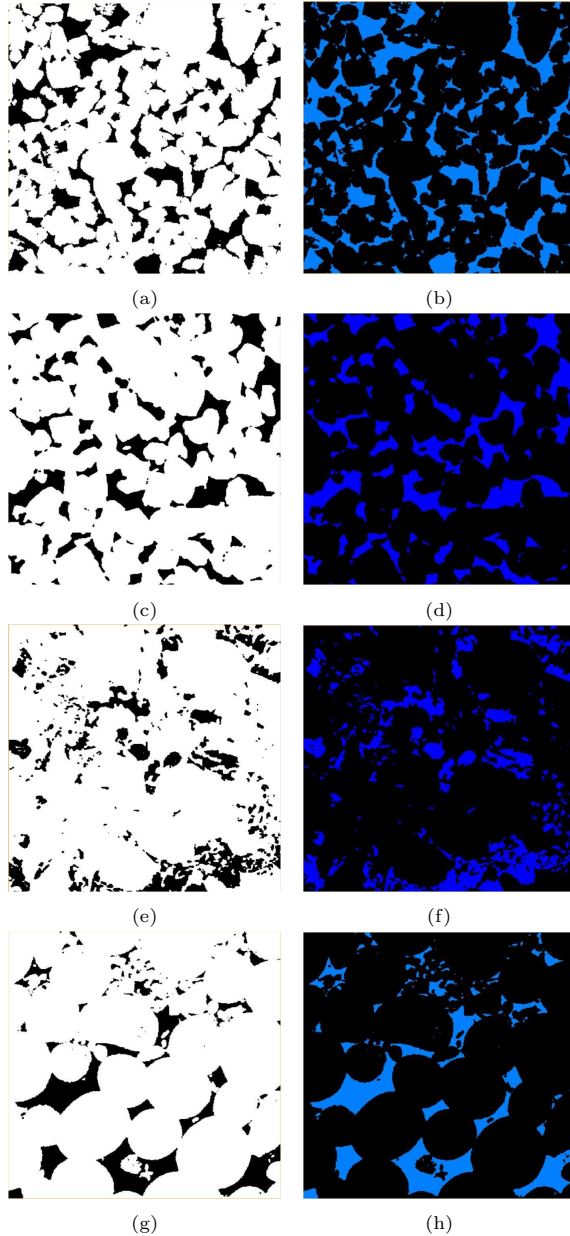


Figure 4: Binary CT images and segmented images, where blue areas are pore spaces and black areas are grain spaces. (a) and (b) Bentheimer sandstone; (c) and (d) Doddington sandstone; (e) and (f) Estallades carbonate; (g) and (h) Ketton carbonate.

Table 5: Segmentation data

Material	Voxel size (μm)	Resolved porosity (%)
Bentheimer sandstone	3.0	21.4
Doddington sandstone	2.7	19.4
Estallades carbonate	3.3	12.4
Ketton carbonate	3.0	12.6

large voluminous as well as narrow expansive voids. The distribution of volumes and shapes requires a quantitative analysis.

The statistical analysis of microstructural features, grains and voids, assumed that a feature had to occupy at least three voxels in each spatial direction for a reliable resolution of its geometry. Therefore features occupying less than 27 voxels were excluded from the statistics; this did not affect grains, but only very small voids in some of the rocks. The resulting statistic, frequency and cumulative probability of grain and void volumes for Bentheimer sandstone is shown in Figure 6. This rock will be used as an example of the process of model construction. The corresponding statistics for the other three rocks is given in Appendix A.

The microstructural features, grains and voids, were classified using ratios between their spatial extensions determined by Avizo - largest (L), intermediate (I), and smallest (S). Thin long features, characterised by $I/L < 0.35$, were not found in the images of the four considered rocks. Voluminous features were characterised by $S/L > 0.64$. This criterion classified all grains included in the statistics in Figure 6, as well as in the other three rocks, as voluminous. In order to keep the range of volumes of voluminous features within reasonable limits for model construction,

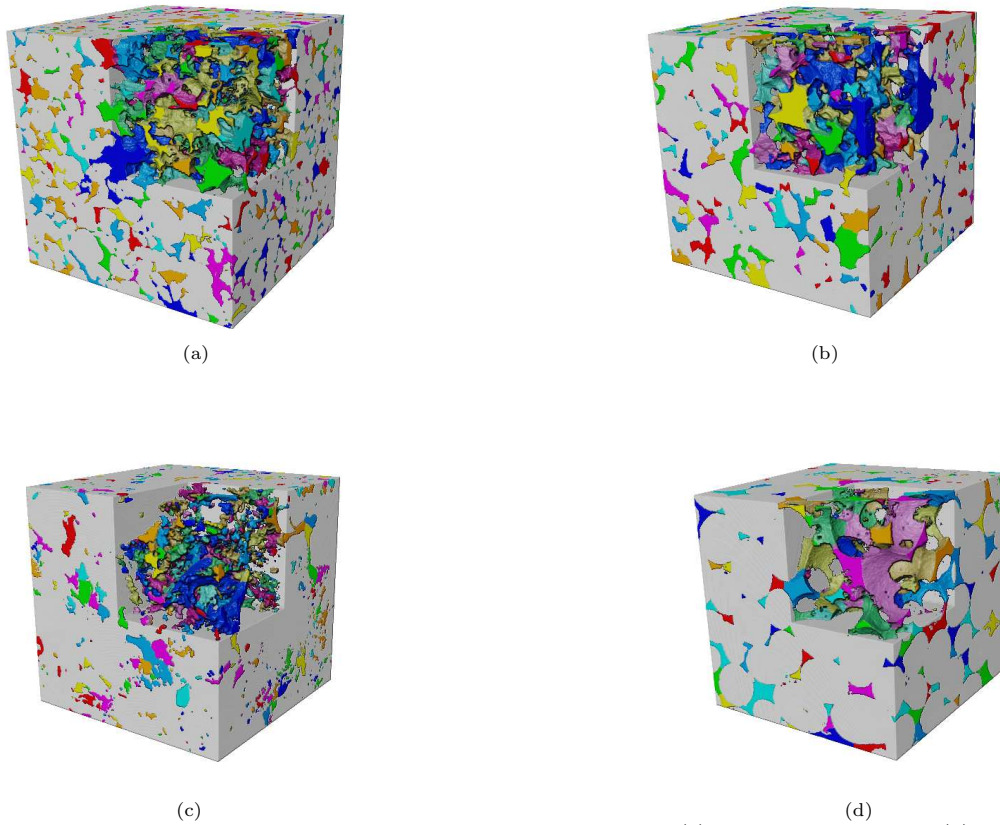


Figure 5: Reconstructed 3D material domains and pore systems based on CT images: (a) Bentheimer sandstone; (b) Doddington sandstone; (c) Estailades carbonate; (d) Ketton carbonate.

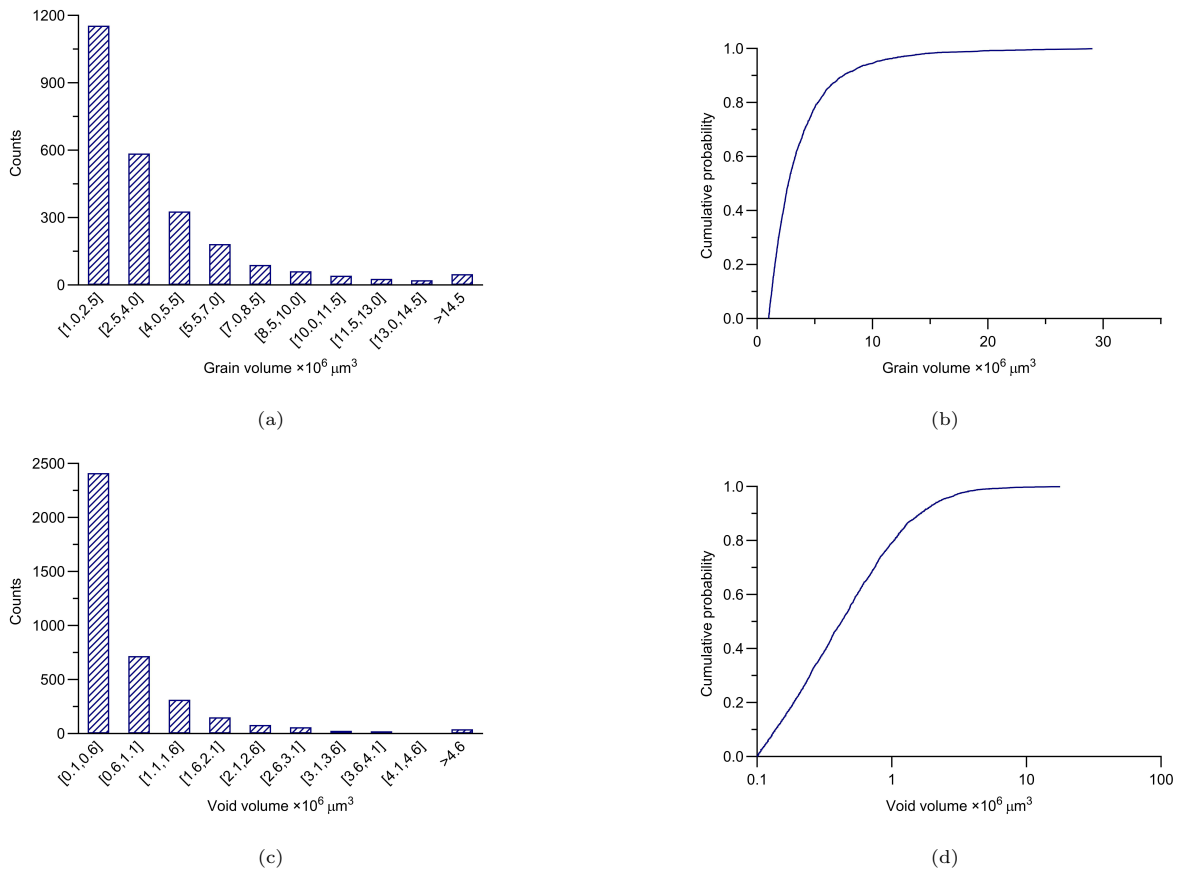


Figure 6: Frequency and cumulative probability of resolved grains (a, b) and voids (c, d) in Bentheimer sandstone.

the voids were first separated into two classes, smaller and larger, than the smallest grain. The voids in the first class were assumed to be expansive, while the voids in the second class were classified into voluminous or expansive based on the same criterion used for grains. The voluminous voids were added to the grain volume frequency to obtain

the frequency of voluminous features for model construction, shown in Figure 7a. The cumulative probability of the remaining voids, considered expansive, is shown in Figure 7b.

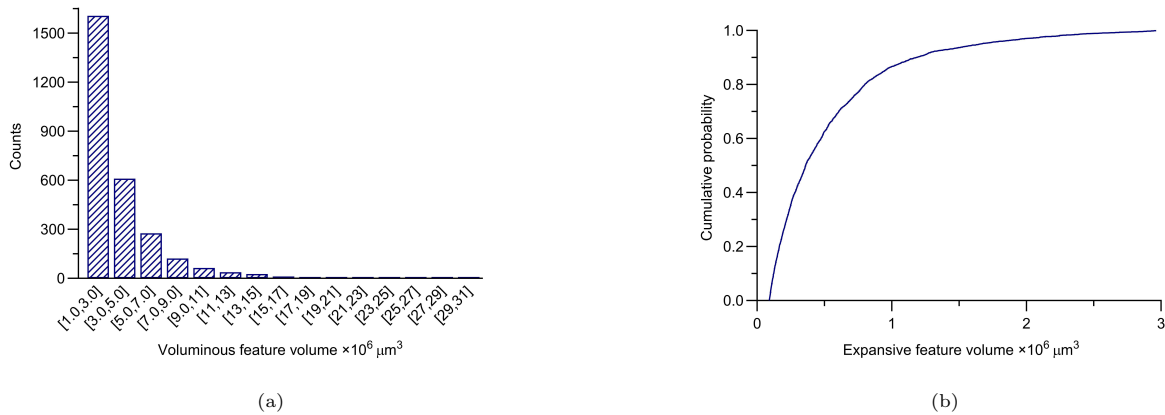


Figure 7: (a) Frequency of voluminous microstructural features (grains and large voids) and (b) cumulative probability of expansive microstructural features (small and large voids) in Bentheimer sandstone.

3.2. Models construction

The microstructures of a rock was represented by a cell complex, \mathcal{M} , constructed by the open-source software Neper (<https://neper.info>), which was developed for modelling polycrystalline assemblies [28]. In our case, the statistical distribution of volumes of voluminous features, grains and large voluminous voids, shown in Figure 7a, was given to Neper as input to generate a tessellation of a cubical domain into polyhedral cells with the same volume distribution. The output from Neper was the full geometrical and topological information about the cell complex \mathcal{M} . The microstructural features were mapped to the corresponding cells of \mathcal{M} - grains and voluminous voids to 3-cells, and narrow expansive voids to 2-cells. A schematic of the process is shown in Figure 8. The mapping of voluminous voids to 3-cells was performed by selecting 3-cells with the closest possible volumes, so that the total volume of voids in this class equaled the volume of voids included in Figure 7b. We note that the 2-cells on the boundaries of 3-cells associated with voluminous voids were excluded from subsequent distribution of expansive voids. The mapping of expansive voids to 2-cells was performed by two random processes. First, a uniform random number $0 < p < 1$ was generated and the corresponding void volume was determined from Figure 7b. Second, a 2-cell was selected at random from the set of 2-cells with no prior association with an expansive void or a boundary of an voluminous void. The mapping of expansive voids to 2-cells was terminated when the total volume fraction of all assigned voids equaled the rock's void volume fraction.

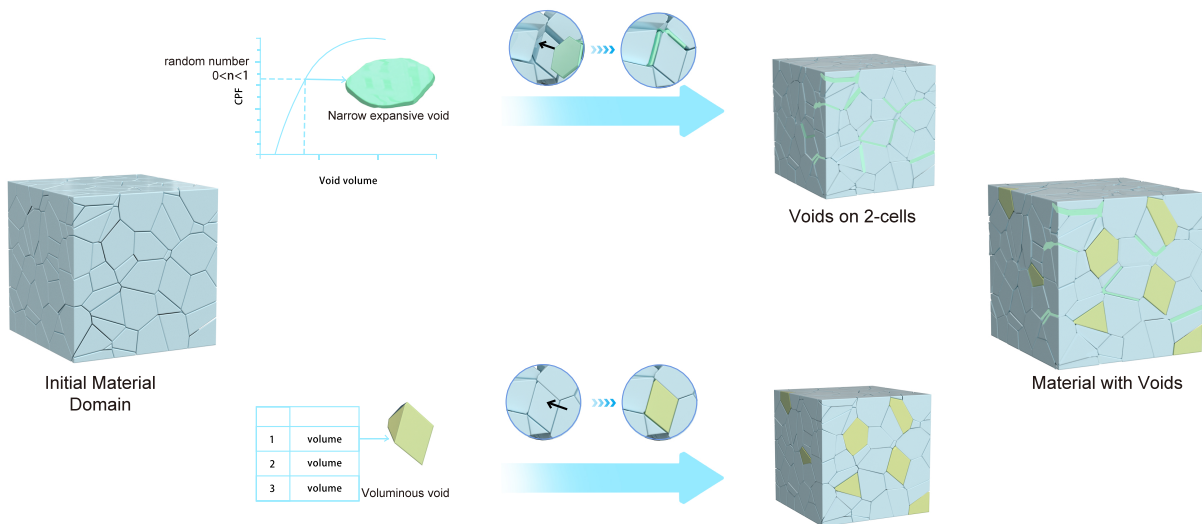


Figure 8: Illustration of pore allocating process.

The output was used by our in-house software to generate the computational complex \mathcal{K} , whose material properties were assigned as follows. A 3-cell in \mathcal{M} with mapped pore was declared conductive through the interior, along its 2-cell boundaries and its 1-cell boundaries, while a 2-cell in \mathcal{M} was declared conductive along its surface and along its 1-cell boundaries. Thus the 1-cells of \mathcal{K} corresponding to the pairs $(c_0 \prec c_1)$, $(c_1 \prec c_2)$ and $(c_2 \prec c_3)$ of a conductive 3-cell c_3 , as well as the 1-cells of \mathcal{K} corresponding to the pairs $(b_0 \prec b_1)$ and $(b_1 \prec b_2)$ of a conductive 2-cell b_2 , were assigned conductivity coefficients for which we used the textbook exact solutions for Poiseuille (pressure-driven) flows

[29]. The solution for the velocity \mathbf{v} of a fluid with dynamic viscosity μ in a cylinder of radius r is

$$\mathbf{v} = \frac{r^2}{8\mu} \nabla p. \quad (32)$$

This was used for calculating the local conductivities of 1-cells in \mathcal{K} corresponding to the pairs $(b_0 \prec b_1)$, $(c_0 \prec c_1)$, $(c_2 \prec c_3)$ as $\pi = r^2/(8\mu)$ with r being the half of h in eq. (33), or the half length from midpoint of c_1 to corresponding c_3 , or the radius of a disk with area equal to the area of c_2 respectively. The solution for the velocity \mathbf{v} of a fluid with dynamic viscosity μ between two plates at distance h is

$$\mathbf{v} = \frac{h^2}{12\mu} \nabla p. \quad (33)$$

This was used for calculating the local conductivities of 1-cells in \mathcal{K} corresponding to the pairs $(b_1 \prec b_2)$ and $(c_1 \prec c_2)$ as $\pi = h^2/(12\mu)$. If b_2 were a 2-cell with mapped expansive void, then h was determined by dividing the volume of the mapped void by the area of b_2 . If b_2 were a 2-cell on the boundary of a 3-cell c_3 with mapped voluminous void, then h was set to the length of the 1-cell in \mathcal{K} corresponding to the pair $(c_2 \prec c_3)$. All remaining 1-cells in \mathcal{K} were assigned very small conductivities, $10^{-12} \text{ m}^2/(\text{Pa}\cdot\text{s})$, to avoid singularity problems. The dynamic viscosity in all cases was taken to be $1.0 \times 10^{-3} \text{ kg}\cdot(\text{m}\cdot\text{s})^{-1}$.

4. Results and discussion

The statistics of voluminous and expansive features was used to create 30 model realisations for each of the four rocks. An example of two different model realisations with the Bentheimer sandstone's statistics is shown in Figure 9. The models were subjected to pressure difference of 1 (Pa) at two opposite faces with the remaining four faces isolated. The pressure distribution calculated with the first realisation at steady-state is shown in Figure 10 to illustrate the heterogeneity of the pressure field dictated by the local conductivities of microstructural features. The plots were created by a natural neighbour interpolation, a three-dimensional algorithm that incorporates neighbouring out-of-plane values into the calculation. As a result, the three planes in the figure provide an in-depth picture of the pressure variation at their intersection and the surroundings. It is worth recalling that pressure values were obtained for all 0-cells in \mathcal{K} . The emergent/macroscopic conductivity and hence permeability values in each of the three directions of the cubical models were calculated for each model realisation, thus providing 90 permeability values for each rock. The average permeability values calculated by the proposed modelling and simulation method are given in the second column of Table 6.

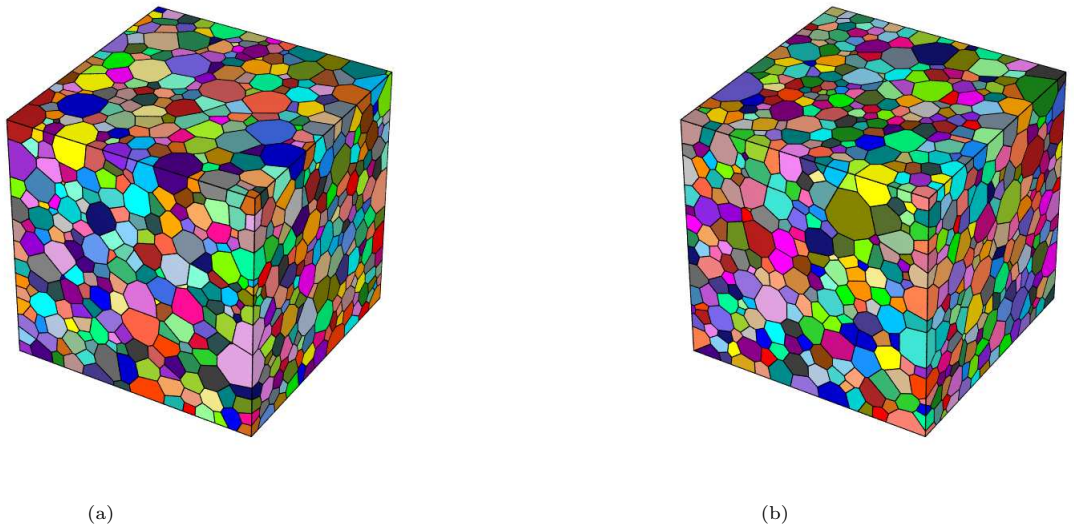
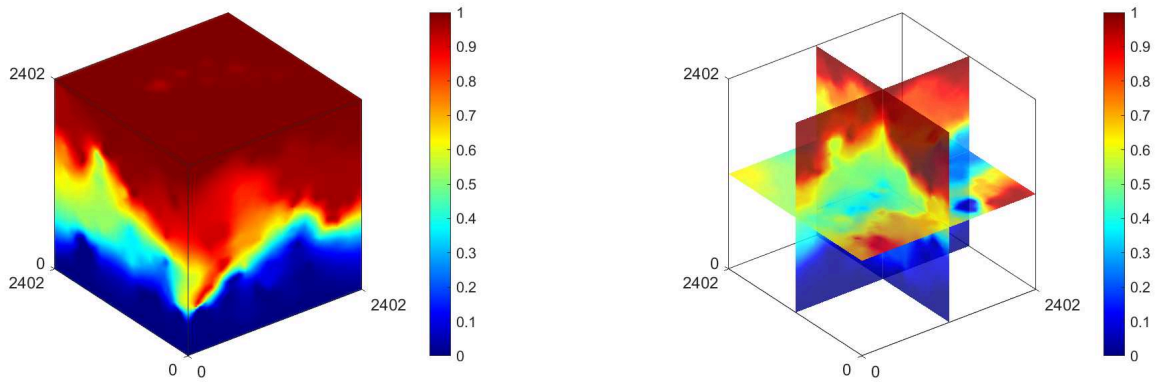


Figure 9: Models of Bentheimer sandstone with the same statistical distributions of features' volumes and different features' spatial arrangements.

In addition, the permeability of the images of the four rocks were calculated by the Absolute Permeability Experiment Simulation, which is a function in XLab Hydro module of Avizo. The calculations in this simulator are realized by solving Navier-Stokes equations in the void space and using Darcy's law to obtain the permeability. The flow equations are solved with the assumptions of incompressible fluid with constant dynamic viscosity (the same as the value used in our models), and laminar flow (the same as the assumption for the local conductivities in our models). The boundary conditions were the same as for the new method with a no-slip condition at fluid-solid interfaces. The boundary pressure difference was set at 1 (Pa) as for the calculations with the new model. The permeability values calculated by Avizo are given in the third column of Table 6.



(a) (b)
Figure 10: Pressure (Pa) distribution in Bentheimer sandstone (μm)

For (partial) validation we include in the fourth column of Table 6 the experimentally measured permeability values [26, 27], noting again that these were obtained with samples of the four rocks larger than the imaged samples. The measurements of Estailades carbonate, Doddington sandstone and Ketton carbonate were conducted at Weatherford Laboratories (East Grinstead, UK) and the measurement of Bentheimer sandstone were conducted at Imperial College (London, UK). In all cases the samples were cylinders with 6.5 mm diameter and 22 mm height.

Table 6: A summary of results for all rock samples

Material	Average permeability from 30 model realisations (10^{-12} m^2)	Single permeability computed by CFD (10^{-12} m^2)	Single experimental permeability (10^{-12} m^2)
Bentheimer sandstone	4.32	6.89	1.875
Doddington sandstone	3.84	6.08	1.038
Estailades carbonate	1.59	2.11	0.149
Ketton carbonate	4.47	5.38	2.807

The results in Table 6 show that the new modelling and simulation method delivers permeability values in good agreement with the classical CFD and with experiments. Figure 11 shows the full sets of calculated permeability values, depicted by dots, the CFD computed values with black solid line, and the measured values with black dashed line for all studied rocks. These results demonstrate two things. First, a comparison of the CFD and experimental values show that the fabrics (statistics and spatial arrangement of voids and grains volumes and shapes) of the segmented images were different from the fabrics of the specimens used for experimental measurement of permeability. Secondly, the proposed modelling approach can take the statistics of grains and voids volumes and shapes and by testing different arrangements predict the spread of the macroscopic property values that is expected for given statistics. The observation that in most cases the experimental values are not within the calculated spread suggest that the statistics extracted from the imaged samples are not the same as for the experimental samples. Improving the statistics, i.e., considering a larger set of imaged samples from the rocks is expected to improve the predictive capability.

It is noted that the local conductivity values assigned to different cells of the cell complex are taken from the solutions of flow in cylindrical and rectangular channels, which is a simplification of the real pore-scale morphologies. One possible approach to account for real morphologies is to consider the void surfaces as having fractal dimensions.

An important advantage of the proposed method is its computational efficiency. We show in Table 7 the average computational resources for a single simulation with the new method and the CFD simulations for the four rocks. It should be noted when making the comparison, that the new method was used on a single PC with a working code written in Matlab, which can be found at https://github.com/changhaoliu-UOM/flow_2024.git, while the CFD was performed on a GPU array, which provides further support for the efficiency of the new formulation.

Table 7: Computational resources required for a single simulation

Material	Memory and CPU time	Memory and GPU time
Bentheimer sandstone	988 MB, 209 sec	50.3 GB, 19 min
Doddington sandstone	445 MB, 78 sec	51.8 GB, 22 min
Estailades carbonate	580 MB, 122 sec	50.6 GB, 21 min
Ketton carbonate	590 MB, 54 sec	53.1 GB, 24 min

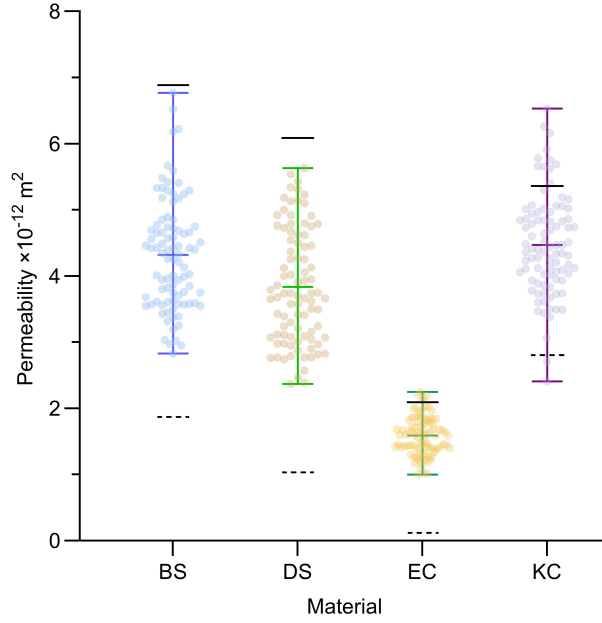


Figure 11: Full set of permeability values of the four rocks

5. Conclusions

We have presented a new foundation for modelling the materials systems where they are represented by cell complexes - collections of cells of different topological dimensions. This is markedly different from the two classical approaches, where materials systems are represented as either finite collections of distinct points (discrete topology) leading to various particle methods, such as molecular dynamics, peridynamics, smoothed particle hydrodynamics, etc., or as infinite collections of infinitesimal points (smooth topology) leading to the continuum description of physics solved by spatial discretisation methods, such as finite elements, finite volumes, finite differences, etc. The advantages of the new modelling foundations are as follows:

- It allows for faithful representation of materials with complex internal structures, where elements with different apparent dimensions may have different material properties and may take part in the physical processes in interaction with others. This feature has been demonstrated in the present work by the construction of models for four rocks using experimentally determined grain and void volume and shape distributions.
- It permits formulations of the conservation laws of physics that respect the underlying structure - the topology and geometry of the cell complex together with the material properties of its components. Importantly, these formulations are directly in matrix form and are exact for a given complex, i.e., the method uses discrete operators in contrast to classical numerical methods which use discretisation of material domains and approximation of continuum operators. This feature has been demonstrated in the present work by the simulation of fluid flow in the models of four rock to calculate their macroscopic property permeability.
- It facilitates investigation of structure-properties relations in materials by linking topological characteristics of sub-structures, e.g., the sub-structures of voids and grains, to calculated macroscopic properties. This feature has not been explored in the present work and is part of ongoing research. Specifically for porous media, such investigation is expected to demonstrate whether the permeability is a function only of the three classical bulk parameters - porosity, tortuosity, and grain surface area - or further parameter(s) are required to capture differences in the arrangement of fabric's features.

The models construction and solutions for flow have shown that:

- The tessellation of domains into polyhedrons using the statistics of voluminous features by Neper creates suitable 3D canvases for introducing all observed features of the materials' fabrics in a sufficiently realistic manner. The algorithm for mapping observed features to elements of the cell complex produces heterogeneous models with specified void and grain volume distributions that can be used for studying the effect of different arrangements of features on the emergent property.
- The calculated permeability values are in good agreement with the CFD calculations and the experimentally measured values for all rocks. The calculated spread of values with different fabrics' arrangements shows that the proposed modelling and simulation method can be used to estimate the variability of a macroscopic property for a given statistics and that the estimation can be improved by improving the input statistics.

- The proposed modelling and simulation method requires an order of magnitude less time and two orders of magnitude less memory than the classical CFD for calculating the macroscopic property permeability.

Importantly, the proposed approach can be used to investigate the evolution of macroscopic properties due to changes in the fabric in a simple and effective way. For example, a non-linear version of the solution method will allow to analyse flow in evolving pore spaces because of different factors, such as dissolution and precipitation, deformation, and fracture propagation. The mathematical formulation is identical for all conservation laws involving scalar potentials (mass density, temperature, electric charge), which allows for seamless coupling of different processes, e.g., fluid flow, mass diffusion, and heat conduction, with different material properties and couplings in different elements of the fabric. The conservation laws for linear and angular momenta, needed for analysis of deformation and fracture, involve (classically) vector potentials, displacement or velocity fields. The discrete versions of these laws require the introduction of discrete bundle-valued differential forms. The development of the corresponding apparatus is analogous to the recently published excellent work on elasticity with smooth exterior calculus [30], and is a subject of ongoing work.

References

- [1] M. B. Allen, *The Mathematics of Fluid Flow Through Porous Media*, John Wiley & Sons, 2021.
URL <https://onlinelibrary.wiley.com/doi/book/10.1002/9781119663881>
- [2] M. G. Larson, F. Bengzon, *The Finite Element Method: Theory, Implementation, and Applications*, Springer Science & Business Media, 2013. doi:10.1007/978-3-642-33287-6.
URL <https://link.springer.com/book/10.1007/978-3-642-33287-6>
- [3] F. Moukalled, L. Mangani, M. Darwish, *The Finite Volume Method in Computational Fluid dynamics*, Springer Science & Business Media, 2016. doi:10.1007/978-3-319-16874-6.
URL <https://link.springer.com/book/10.1007/978-3-319-16874-6>
- [4] L. Holzer, P. Marmet, M. Fingerle, A. Wiegmann, M. Neumann, V. Schmidt, *Tortuosity and microstructure effects in porous media: classical theories, empirical data and modern methods*, Springer Nature, 2023. doi:10.1007/978-3-031-30477-4.
URL <https://link.springer.com/10.1007/978-3-031-30477-4>
- [5] S. Nemat-Nasser, M. Hori, *Micromechanics: overall properties of heterogeneous materials*, North-Holland, 1993.
URL <https://www.sciencedirect.com/bookseries/north-holland-series-in-applied-mathematics-and-mechanics/vol/37/suppl/C>
- [6] A. Costa, *Permeability-porosity relationship: A reexamination of the Kozeny-Carman equation based on a fractal pore-space geometry assumption*, *Geophysical research letters* 33 (2) (2006).
URL <https://agupubs.onlinelibrary.wiley.com/doi/10.1029/2005GL025134>
- [7] J. Sarout, *Impact of pore space topology on permeability, cut-off frequencies and validity of wave propagation theories*, *Geophysical Journal International* 189 (1) (2012) 481–492. doi:10.1111/j.1365-246X.2011.05329.x.
URL <https://academic.oup.com/gji/article-lookup/doi/10.1111/j.1365-246X.2011.05329.x>
- [8] P. Carman, *Flow of Gases Through Porous Media*, Butterworths, 1956.
- [9] T. Chen, M. Sedighi, A. P. Jivkov, S. C. Seetharam, *A model for hydraulic conductivity of compacted bentonite-inclusion of microstructure effects under confined wetting*, *Géotechnique* 71 (12) (2021) 1071–1084. doi:10.1680/jgeot.21.00019.
URL <https://www.icvirtuallibrary.com/doi/10.1680/jgeot.21.00019>
- [10] Z. Wang, M. Sedighi, A. R. Lea-Langton, M. Babaei, *Hydraulic behaviour of sand-biochar mixtures in water and wastewater treatment applications*, *Journal of Hydrology* 612 (2022) 128220. doi:10.1016/j.jhydro.2022.128220.
URL <https://linkinghub.elsevier.com/retrieve/pii/S0022169422007922>
- [11] A. P. Jivkov, Q. Xiong, *A network model for diffusion in media with partially resolvable pore space characteristics*, *Transport in porous media* 105 (2014) 83–104. doi:10.1007/s11242-014-0360-1.
URL <https://link.springer.com/article/10.1007/s11242-014-0360-1>
- [12] Q. Xiong, C. Joseph, K. Schmeide, A. P. Jivkov, *Measurement and modelling of reactive transport in geological barriers for nuclear waste containment*, *Physical Chemistry Chemical Physics* 17 (45) (2015) 30577–30589. doi:10.1039/C5CP05243B.
URL <https://xlink.rsc.org/?DOI=C5CP05243B>

- [13] T. G. Baychev, A. P. Jivkov, A. Rabbani, A. Q. Raeini, Q. Xiong, T. Lowe, P. J. Withers, [Reliability of algorithms interpreting topological and geometric properties of porous media for pore network modelling](#), *Transport in Porous Media* 128 (2019) 271–301.
URL <https://link.springer.com/article/10.1007/s11242-019-01244-8>
- [14] J. Santos, B. Chang, A. Gigliotti, Y. Yin, W. Song, N. Prodanovic, Q. Kang, N. Lubbers, H. Viswanatan, [A dataset of 3d structural and simulated transport properties of complex porous media](#), *Scientific Data* 9 (2022) 579.
URL <https://doi.org/10.1038/s41597-022-01664-0>
- [15] B. Jähne, [Digital image processing](#), 6th Edition, Springer Science & Business Media, 2005. doi:10.1007/3-540-27563-0.
URL <https://link.springer.com/book/10.1007/3-540-27563-0>
- [16] H. C. Liang Xue, Xiaozhe Guo, [Fluid flow in porous media : fundamentals and applications](#), World Scientific, 2021.
URL <https://www.worldscientific.com/worldscibooks/10.1142/11805>
- [17] E. Cartan, [Sur certaines expressions différentielles et le problème de Pfaff](#), in: *Annales scientifiques de l'École normale supérieure*, Vol. 16, 1899, pp. 239–332. doi:10.24033/asens.467.
URL http://www.numdam.org/item/?id=ASENS_1899_3_16__239_0
- [18] D. Bachman, [A Geometric Approach to Differential Forms](#), Springer Science+Business Media, 2012.
URL <https://doi.org/10.1007/978-0-8176-8304-7>
- [19] J. P. Fortney, [A Visual Introduction to Differential Forms and Calculus on Manifolds](#), Springer Nature Switzerland AG, 2018.
URL <https://doi.org/10.1007/978-3-319-96992-3>
- [20] K. Berbatov, P. D. Boom, A. L. Hazel, A. P. Jivkov, [Diffusion in multi-dimensional solids using Forman's combinatorial differential forms](#), *Applied Mathematical Modelling* 110 (2022) 172–192. doi:10.1016/j.apm.2022.05.043.
URL <https://www.sciencedirect.com/science/article/pii/S0307904X22002657>
- [21] S. O. Wilson, [Cochain algebra on manifolds and convergence under refinement](#), *Topology and its Applications* 154 (9) (2007) 1898–1920. doi:10.1016/j.topol.2007.01.017.
URL <https://www.sciencedirect.com/science/article/pii/S0166864107000314>
- [22] R. F. Arnold, [The discrete Hodge star operator and Poincaré duality](#), Ph.D. thesis, Virginia Tech (2012).
URL <https://vtechworks.lib.vt.edu/handle/10919/27485>
- [23] L. Ptáčková, [A discrete wedge product on polygonal pseudomanifolds](#), Ph.D. thesis, Instituto de Matemática Pura e Aplicada (2017).
URL https://www.visgraf.impa.br/Data/RefBib/PS_PDF/student-phd-2017-02-lenka-ptackova/FinalThesis.pdf
- [24] R. Forman, [Combinatorial Novikov-Morse theory](#), *International Journal of Mathematics* 13 (4) (2002) 333–368. doi:10.1142/S0129167X02001265.
URL <https://www.worldscientific.com/doi/abs/10.1142/S0129167X02001265>
- [25] K. Berbatov, [Discrete approaches to mechanics and physics of solids](#), Ph.D. thesis, The University of Manchester (2023).
URL https://pure.manchester.ac.uk/ws/portalfiles/portal/261212897/FULL_TEXT.PDF
- [26] A. Q. Raeini, B. Bijeljic, M. J. Blunt, [Generalized network modeling: Network extraction as a coarse-scale discretization of the void space of porous media](#), *Physical Review E* 96 (1) (2017) 013312. doi:10.1103/PhysRevE.96.013312.
URL <https://journals.aps.org/pre/abstract/10.1103/PhysRevE.96.013312>
- [27] M. Andrew, [Reservoir-condition pore-scale imaging of multiphase flow](#), Ph.D. thesis, Imperial College London (2014). doi:10.25560/24915.
URL <https://spiral.imperial.ac.uk/handle/10044/1/24915>
- [28] R. Quey, P. R. Dawson, F. Barbe, [Large-scale 3d random polycrystals for the finite element method: Generation, meshing and remeshing](#), *Computer Methods in Applied Mechanics and Engineering* 200 (17-20) (2011) 1729–1745. doi:10.1016/j.cma.2011.01.002.
URL <https://linkinghub.elsevier.com/retrieve/pii/S004578251100003X>

[29] C. Fang, *An Introduction to Fluid Mechanics*, Springer International Publishing AG, 2019.
 URL <https://doi.org/10.1007/978-3-319-91821-1>

[30] R. Rashad, A. Brugnoli, F. Califano, E. Luesink, S. Stramigioli, *Intrinsic nonlinear elasticity: An exterior calculus formulation*, *Journal of Nonlinear Science* 33 (2023) 84. doi:10.1007/s00332-023-09945-7.
 URL <https://doi.org/10.1007/s00332-023-09945-7>

Appendix A. Statistics of resolved features in rocks

The statistics of the resolved microstructural features and those used for constructing the models of the remaining three rocks are shown in the following figures: Doddington sandstone (Figure A.12, Figure A.13), Estailades carbonate (Figure A.14, Figure A.15) and Ketton carbonate (Figure A.16, Figure A.17).

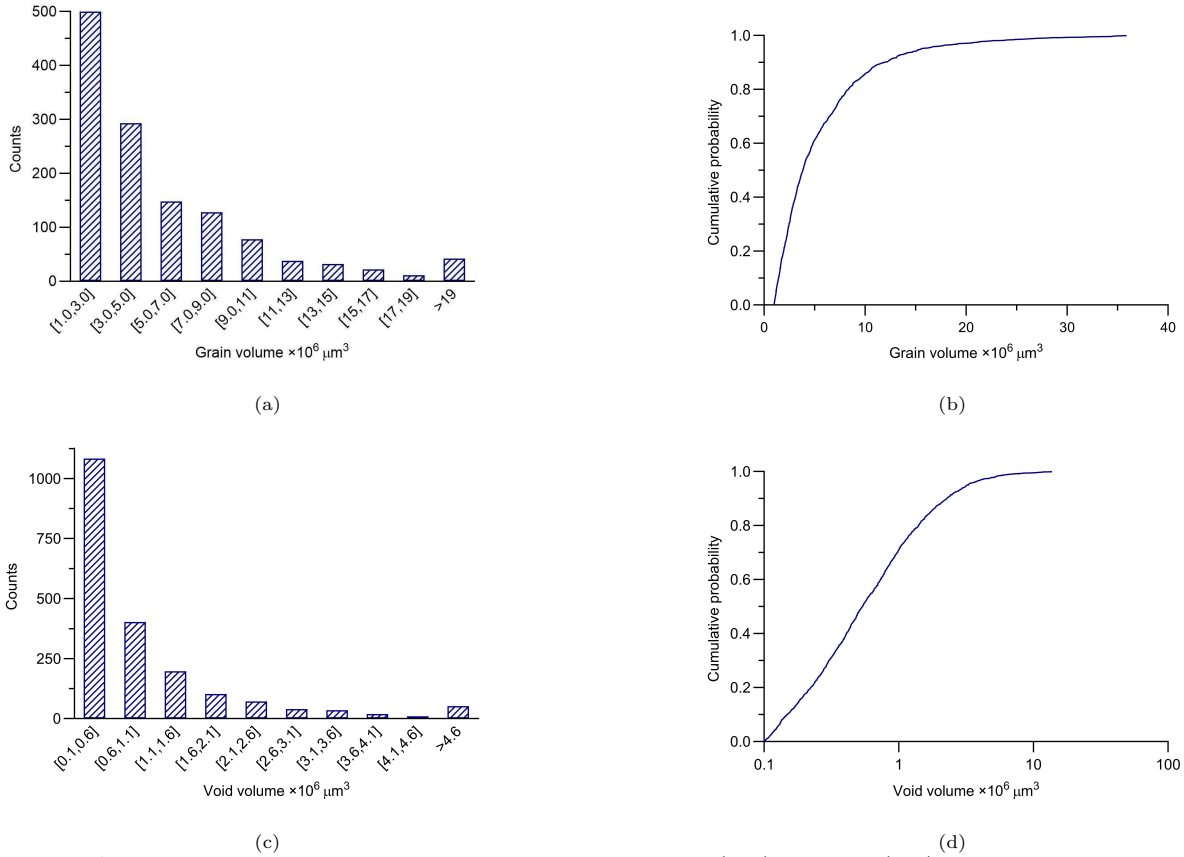


Figure A.12: Frequency and cumulative probability of resolved grains (a, b) and voids (c, d) in Doddington sandstone

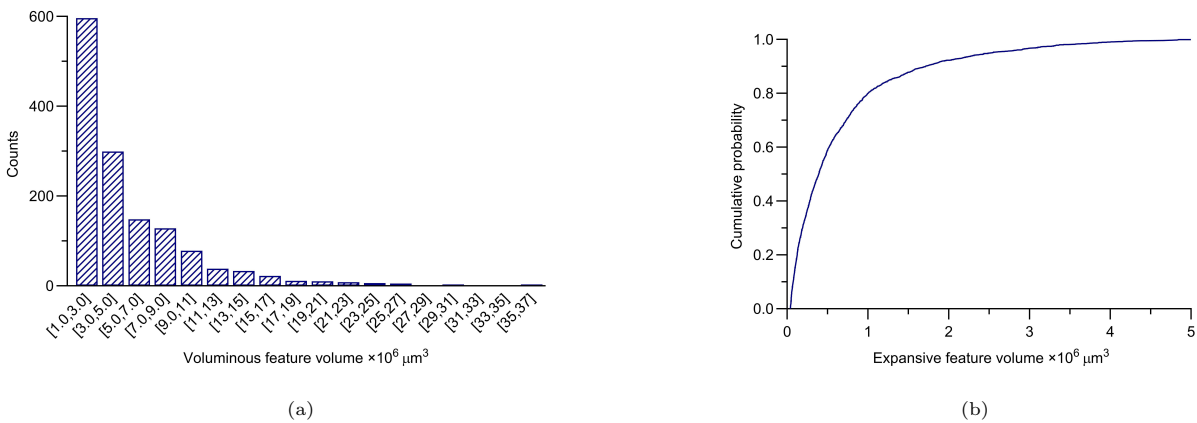
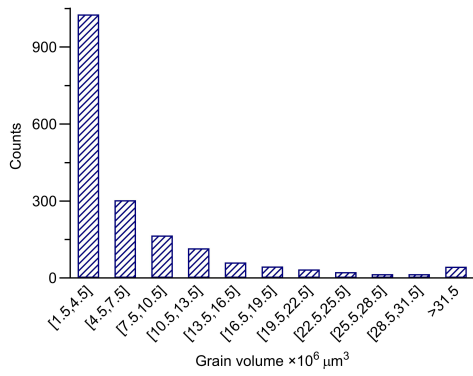
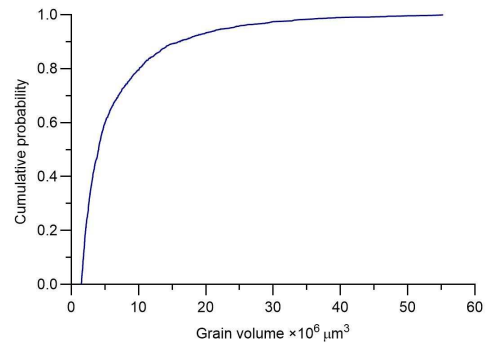


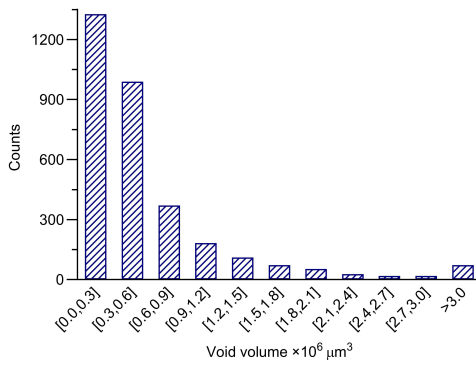
Figure A.13: (a) Frequency of voluminous microstructural features (grains and large voids) and (b) cumulative probability of expansive microstructural features (small and large voids) in Doddington sandstone



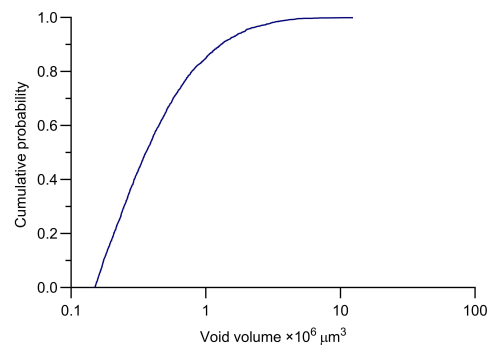
(a)



(b)

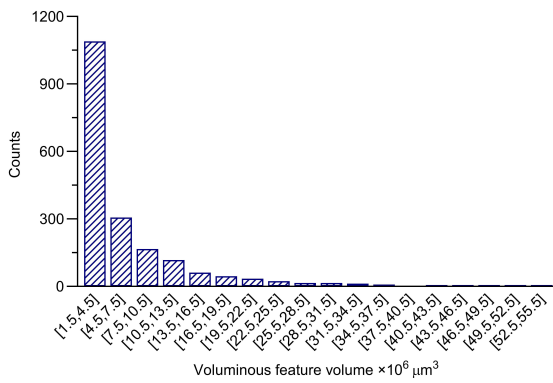


(c)

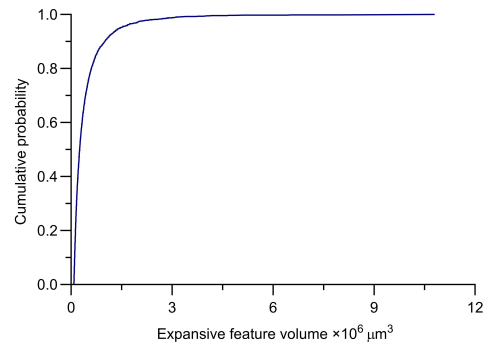


(d)

Figure A.14: Frequency and cumulative probability of resolved grains (a, b) and voids (c, d) in Estailades carbonate

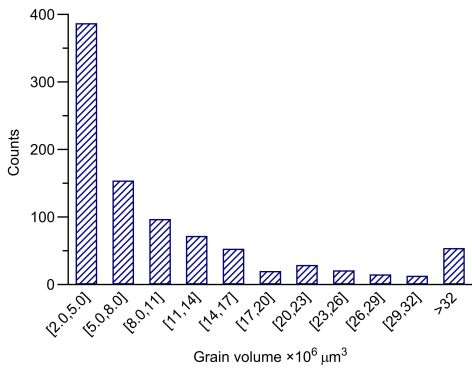


(a)

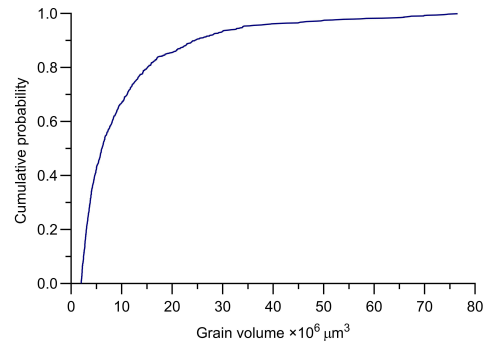


(b)

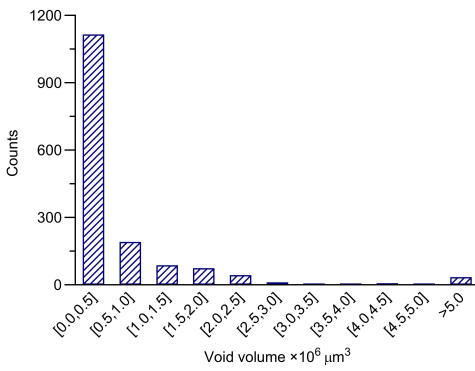
Figure A.15: (a) Frequency of voluminous microstructural features (grains and large voids) and (b) cumulative probability of expansive microstructural features (small and large voids) in Estailades carbonate



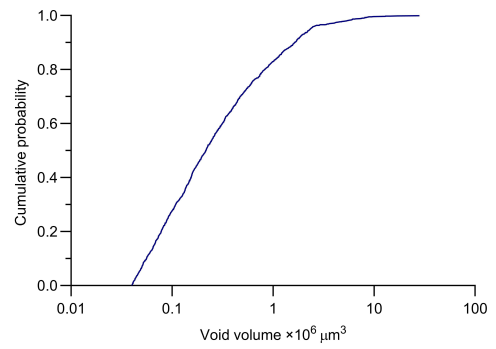
(a)



(b)

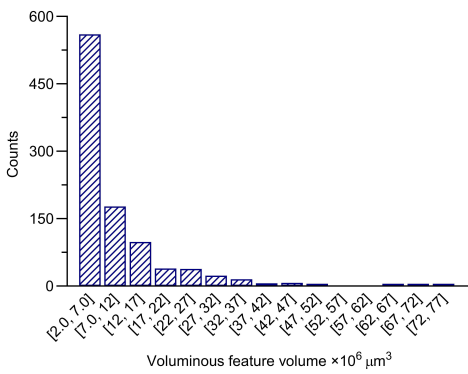


(c)

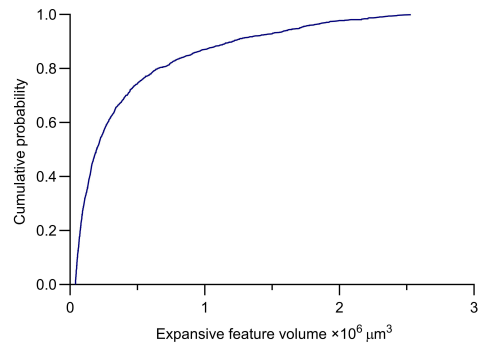


(d)

Figure A.16: Frequency and cumulative probability of resolved grains (a, b) and voids (c, d) in Ketton carbonate



(a)



(b)

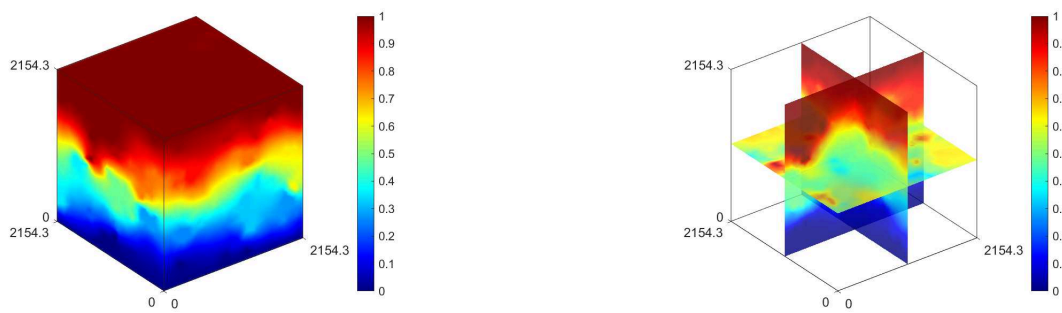
Figure A.17: (a) Frequency of voluminous microstructural features (grains and large voids) and (b) cumulative probability of expansive microstructural features (small and large voids) in Ketton carbonate

Appendix B. Examples of model realisations and pressure solutions for rocks

Two model realisations and one calculated pressure distribution are shown in the following figures: Doddington sandstone (Figure B.18, Figure B.19), Estailades carbonate (Figure B.20, Figure B.21) and Ketton carbonate (Figure B.22, Figure B.23).



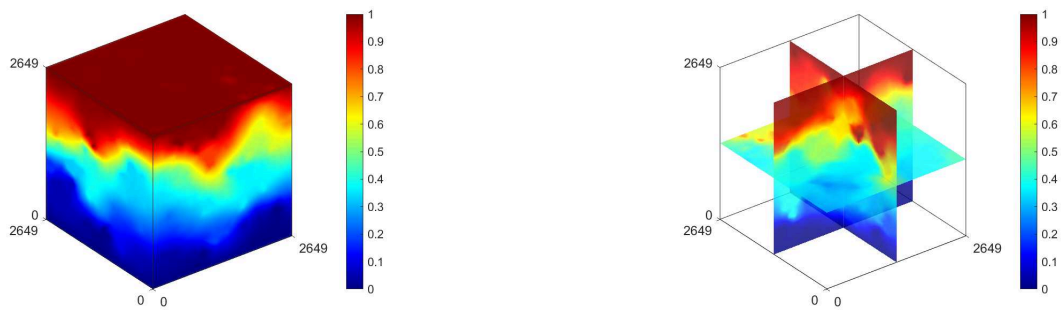
(a) (b)
Figure B.18: Reconstructed cubical meshes of Doddington sandstone



(a) (b)
Figure B.19: Pressure (Pa) distribution in Doddington sandstone (μm)



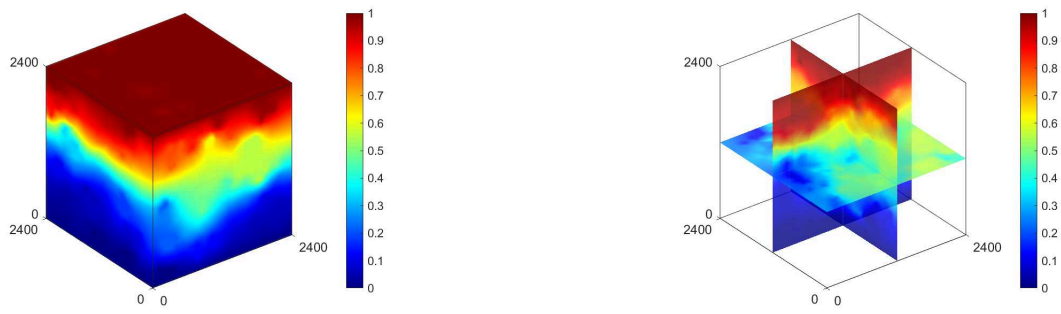
(a) (b)
Figure B.20: Reconstructed cubical meshes of Estailades carbonate



(a) (b)
 Figure B.21: Pressure (Pa) distribution in Estallades carbonate (μm)



(a) (b)
 Figure B.22: Reconstructed cubical meshes of Ketton carbonate



(a) Figure B.23: Pressure distribution (Pa) in Ketton carbonate (μm) (b)